PIERRE AND MARIE CURIE UNIVERSITY OF PARIS

MASTER THESIS

ZrO_2 For ITER first mirrors

Author:
Zakaria AZDAD

Supervisor:
Prof. Ernst MEYER
Dr. Laurent MAROT

A thesis submitted in fulfilment of the requirements
for Master degree in Material Science and Nano-Objects

in the

Nanolino Meyer Group
Department of Physics

October 22, 2015

Declaration of Authorship

I, Zakaria AZDAD, declare that this thesis titled, 'ZrO_2 For ITER first mirrors' and the work presented in it are my own. I confirm that:

- This work was done wholly or mainly while in candidature for a research degree at this University.
- Where any part of this thesis has previously been submitted for a degree or any other qualification at this University or any other institution, this has been clearly stated.
- Where I have consulted the published work of others, this is always clearly attributed.
- Where I have quoted from the work of others, the source is always given. With the exception of such quotations, this thesis is entirely my own work.
- I have acknowledged all main sources of help.
- Where the thesis is based on work done by myself jointly with others, I have made clear exactly what was done by others and what I have contributed myself.

Signed:

Date:

"There are only two ways to live your life. One is as though nothing is a miracle. The other is as though everything is a miracle."

Albert Einstein

PIERRE AND MARIE CURIE UNIVERSITY OF PARIS

Abstract

University of Basel
Department of Physics

Master degree in Material Science and Nano-Objects

ZrO_2 For ITER first mirrors

by Zakaria AZDAD

Metallic First Mirrors (FMs) are the core part of the optical diagnostics in the International Thermonuclear Experimental Reactor (ITER). It is extremely important that the high reflectivity of the mirrors stays constant during the plasma exposure in the harsh ITER environment. More precisely, the FMs are going to be subject to erosion and/or deposition and high neutron bombardment . ZrO_2 is the most radiation resistant ceramic currently known and due to its high transparency, it is interesting to use it as a protective coating for high reflective materials. The optimization of the optical and electronic properties of ZrO_2 to suit ITER criteria are the subject of this present study. In order to select the best film properties, pulsed DC and radio-frequency reactive magnetron sputtering are used to deposited ZrO_2 thin film. The influence of Ar sputtering on the optical and electronic properties are also presented. The characterisation of the deposits were carried out by the mean of ellipsometry, X-ray diffraction, Scanning Electron Microscopy Atomic Force Microscopy, UV-Vis, Insitu X-ray Photoelectron Spectroscopy and Ultraviolet Photon Spectroscopy.

Acknowledgements

This work has been carried out in the context of Contract ID F4E-OPE-649 which has been funded with support from Fusion from Energy. The opinions expressed are those of Contractor only and do not represent Fusion for Energy′s official position.

The Swiss Federal Office of Energy, the Federal Office for Education and Science, the Swiss National Foundation (SNF) and the Swiss Nanoscience Institute (SNI) are acknowledged for their financial support.

This work has been carried out within the framework of the EUROfusion Consortium and has received funding from the European Union's Horizon 2020 research and innovation programme under grant agreement number 633053. The views and opinions expressed herein do not necessarily reflect those of the European Commission.

Contents

Chapter 1

Introduction

1.1 Motivation

Much like quantum computers, the nuclear fusion reactor represent one of the greatest challenge of our modern time. To build such a reactor and to demonstrate the ability of nuclear fusion reaction on a large scale , the project ITER (International Thermonuclear Experimental Reactor) has been launched in collaboration between six states (USA, Japan, Russia, Europe, China, Korea and India). It is not only a matter of exploring the amount of sustainable energy that this reactor will give access to, but it is also a matter of understanding at a fundamental level the physics of plasma fusion that is governed in most of the stars and galaxies around us.

Nevertheless, in order to analyse the plasma inside the reactor it is out of question to perform a direct measurement through a vacuum window due to the large amount of radiations and neutrons flux. To overcome this problem, the measurement will be done using metallic mirrors that will be merged inside the reactor. Using high reflectivity of those mirrors, the light emitted from the plasma will be guided through an optical path to the diagnostic system .

Obviously, the so called "First Mirror" (FM) will undergo intensive contamination by the products of plasma-induced erosion of the plasma facing components. The re-deposition of the wall elements on the mirror will decrease their optical properties . Since accessing to the inside of the reactor to replace them is not an option, an in-situ methods has to be developed to remove the deposited elements from the walls of the reactor (mainly Be and W) on the mirror . Several studies has been done using either laser or plasma cleaning but until now no reliable solution has been approved. The cleaning process is not the only issue, the choice of the materials for the FM's turned out to be a difficult task. Several material have been intensively studied in the literature ; single crystalline molybdenum (ScMo), polycrystalline molybdenum (PcMo), nano-crystalline molybdenum (NcMo) and Rhodium (Rh). For laser cleaning method it has been shown that the redeposited elements were successfully removed without causing any serious damage to mirror and recovering the initial optical properties for the NcMo mirrors. For other materials mentioned the initial optical properties were not completely recovered. It should be point out that in the case of Rh , it was observed that the film might de-laminate completely or show blistering on the surface[59]. In addition the re-deposition of Be in JET (Joint European Torus) facilities showed a non uniformity [26] which might be the case for ITER.

The Plasma cleaning method has shown a promising results [40] with optimized parameters and since it is relatively easy to implement inside ITER, this later is closest to be applied. The validation of this vision will be the main purpose of this project. ZrO_2 in nuclear industry is widely used due its high radiation-resistance and high transparency , it is choose to combine these properties to coat Al film. Because the

access to Be deposition facilities is not possible due to it high toxicity, Al-W and Al_2O_3 films are used to simulate deposition that could take place inside of ITER. Different gas will be tested on both uniform and non uniform layers and for several cycle cleaning.

Different characterization techniques are used to study the deposited films. The chemical composition are performed using in-situ XPS (X-ray Photo-emission Spectroscopy) and UPS (Ultraviolet Photo-electron Spectroscopy) and ex-situ EDX (Energy Dispersive X-Ray spectroscopy). The optical properties are investigated using ellipsometry and Spectrophotometry UV-Vis methods, while the structural studies are conducted using XRD (X-ray diffraction), SEM (Scanning Electron Microscope) and AFM (Atomic Force Microscope.

In the following section a brief introduction to the different techniques used during this project are given. A main focus will be on the used of X-ray photoelectrons spectroscopy , auger lines theory and ellipsometry.

Chapter 2

Thin film deposition using magnetron sputtering

Sputtering deposition is a widely used technique in industry due to it's high deposition rate, film uniformity and the ability to scale up for large area deposition. The deposition using sputtering techniques usually for most application do not require the use of high temperature which reduce significantly the cost of the produced devices. An other attractive property of this technique is that deposition of multi-layer can be reached by only changing the nature of the target which allows the process to be fast. Furthermore the addition of several reactive gases allows to tune the properties of the desirable material and enhance their performances. In this section we will describe direct current (DC) and dadio-frequency (RF) magnetron sputtering and reactive magnetron sputtering , since both of the techniques are used in this project.

2.1 Sputtering process : basic concept

The basic idea behind the sputtering process can be described as the ejections of atoms from a surface as consequence of collisions between a projectile and/or recoil atoms produced and the atoms in the near-surface layers of a target material. Under relatively high vacuum the ejected atom are condensed on a substrate or any surface encountered.

Argon is widely used as gas for sputtering atoms from the surface because of the chemical and physical properties that exhibits. Being a noble gas gave it the properties of not reacting with the surface of the sputtered material and easily ionized when a electrical discharge is applied. While the average mass of argon allows it to sputter all elements with efficiency. A fundamental parameter describe the sputtering process is referred to as the sputtering yield. It is defined as the ratio between the number of ejected atoms and the number of incident particles (projectile). The well known Yamamura formula [36][62] which describe the energy dependency of sputtering yield $Y(E)$ of monoatomic solids for normal incidence of projectiles, is given by :

$$Y(E) = 0.042 \frac{Q(Z_2)\alpha^*(\frac{M_2}{M_1})}{U_s} \frac{S_n(E)}{1 + \Gamma k \epsilon^{0.3}} [1 - \sqrt{\frac{E_{th}}{E}}]^s \tag{2.1}$$

where E is projectile energy , M_1 and M_2 are the masses of a projectile and target atom in a.m.u, and the numerical factor is given in units of Å^{-2}. The Γ has the form of $\Gamma = \frac{W(Z_2)}{1+(M_1/7)^3}$. U_s refers to a surface binding energy,$W(Z_2)$, $Q(Z_2)$ and s are dimensionless parameters tabulated in [63]. The α^* is a function of a mass ratio M_1/M_2, E_{th} is the sputtering threshold energy and S_n is the nuclear stopping cross section. ϵ is the reduced loss energy usually named as LSS

Obviously the Yamamura formula (2.1) is influenced by several factors. The use of light elements to sputter heavy elements will induce a very low sputtering yield. The surface energy plays an essential role. Since it depend on crystallographic direction, the sputtering yield of a polycrystalline target will cause the ejection of atoms at different energies this is illustrated in figure 2.1 extracted from [43]

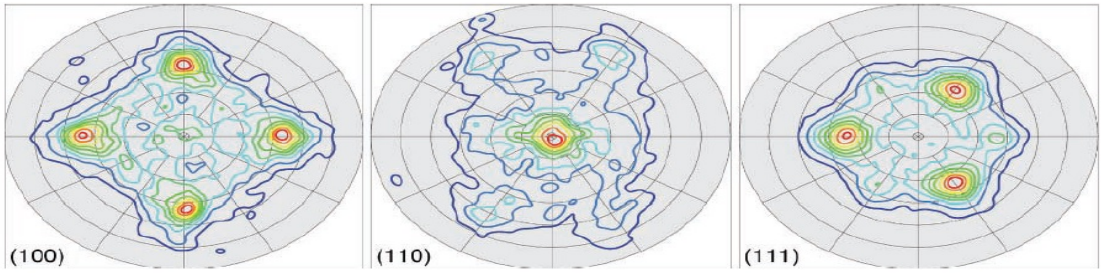

FIGURE 2.1: Spot patterns of sputtered Cu atoms for 5 keV Ar+ impact on Cu (100),(110), and (111) surfaces. Radial and rotational axes correspond to the polar and azimuth angles, respectively. Lines in nine colors from dark grey to light grey indicate contour lines from 10 to 90% with increment of 10%, of the maximum differential sputtering yield

The threshold energy also strongly depend on the particular sputtering collision sequence involved. A general trend of the Y(E) function is illustrated in figure 2.2. In the low energy region near the threshold, the function Y(E) behave as Y(E)$\propto E^2$. As the energy increase and reach 100 eV, Y(E) become proportional to E . In this region, the incident ions collide with the surface atoms of the target, therefore the number of displaced atoms due to the collision will be close to the incident energy. At higher ion energies in the range of 10 to 100 keV, the incident ions penetration depth increases and the sputtering yield is not governed by surface scattering but by bulk scattering. Above 100 keV the sputtering yield decrease due to the energy dissipation of the incident ions deep in the the target.

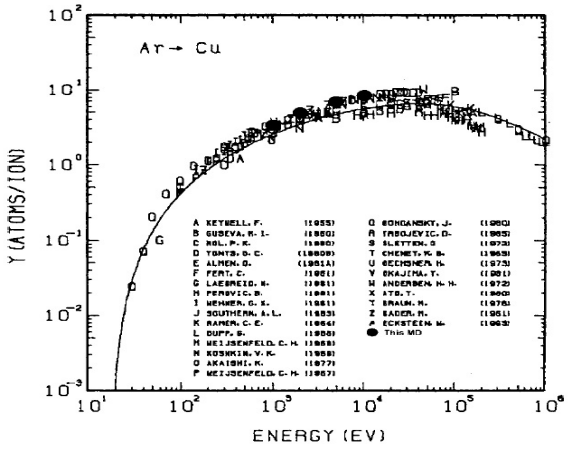

FIGURE 2.2: Energy dependence of Ar^+ ions incident on Cu obtained with experiments, Molecular Dynamic calculations and Yamamura formula [43]

2.1.1 Plasma deposition technique

We saw that the energy of incident ions is an important parameter in Yamamura formula. The use of different sputtering technologies relies on the fact that the ions energies and densities are different, giving the deposited films different properties. The use of DC magnetron sputtering is commonly applied to metallic targets. However for insulator and semiconductors targets and even for reactive magnetron sputtering the DC method turn out to have a strong disadvantage. Due to the high mobility of the electron with respect to ions in the plasma, the electrons are accumulated on the target which causes the attraction of the ions, therefore a continuous sputtering process occur and since the target is conductor its prevent the target from positive charge accumulation . However, where an insulator target is employed, the effect of charge accumulation is strong which causes a development of an electric field that prevent the attraction of ions and thus a stop in the sputtering process. Instead, pulsed DC and RF are frequently employed to sputter insulating materials. In this paragraph a brief overview of the two methods is given.

Plasma discharge

To better describe the sputtering deposition system a brief introduction to glow discharge working principal is necessary because all energetic particles are initially created in the plasma.

To initiate a plasma a minimum voltage is needed : breakdown voltage given by Paschen´ s Law :

$$V_s = a\frac{pl}{log(pl)+b} \tag{2.2}$$

where p is the gas pressure , l is the distance between the electrodes, a and b are constant. The derivative of equation (2.2) with respect to p (dV/dp) gives a minimum breakdown voltage value at a gas pressure noted p_m. In typical sputtering systems the gas pressure is kept below the pressure p_m. To initiate the discharge, the gas pressure p_s under a given electrode distance is given by :

$$p_s \geq \frac{\lambda_0}{l} \tag{2.3}$$

where λ_0 defined the mean free path of electrons in the discharge gas. Typical value of λ_0 for Ar at 100 eV is 0.05 cm. By setting l=0.7 cm the pressure needed to initiate the plasma is $9.3\times10^{-2}mbar$. Clearly we see that the pressure and the spacing between the electrodes plays a significant role. The use of different gases for sputtering changes the initial conditions to start a plasma , because of the difference in the ionization energy and the elastic collision cross section between the electrons and the gas molecules. In general the ionization process in the plasma discharge can be described as follows: the collision between the electrons and the molecules atoms initiate first ions (only possible if the energy of the electrons are higher than the ionization energy of the molecules). At the first stage the primary electrons which are the electrons ejected by the background cosmos radiation are accelerated by the electric field near the cathode. The collisions of these electrons on the way to the electrode with the gas molecules gives rise to ions. The ions are then attracted to the cathode. The bombardment of the cathode surface generates a secondary electrons from the surface, which in their way to the anode create new ions and generate a self-sustained discharge.

This basic introduction to the plasma discharge will give enough tools to describe the pulsed DC and RF discharge. Several other interesting phenomena such as equilibrium conditions, discharge types (Townsend, glow , abnormal etc..) , the appearance of dark region in the plasma etc... are not presented here and the reader can refer [32] for more detailed description.

Pulsed DC deposition

One of the earliest solution to prevent the immediate build-up of a surface charge of positive ions on the front side of the insulator is the used of a pulsed. The generation of the pulses is performed as follows : an inductor is charged by the opening the switch . By closing the switch , the inductor current is diverted to the plasma. When the switch is open a partially decay plasma , the negative voltage rise quickly which increase the power delivered to the plasma this process allows the generation of rectangular signal as seen in figure 2.3a.

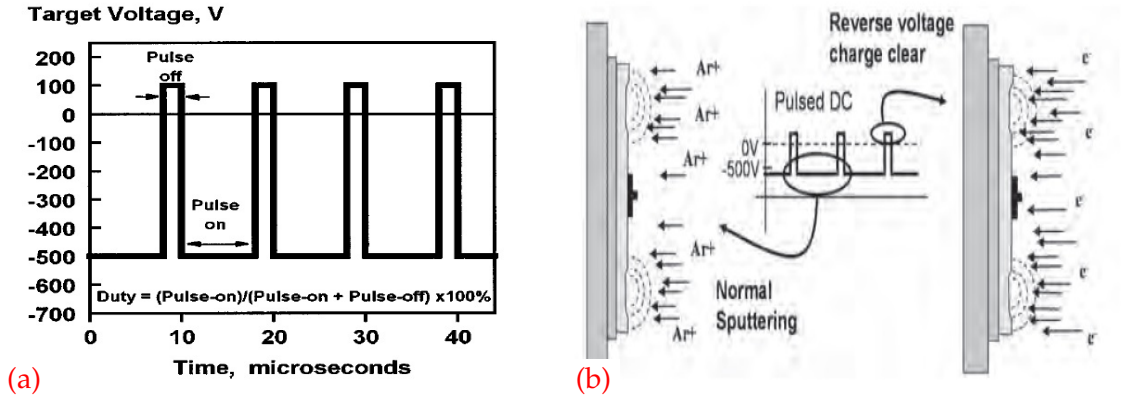

FIGURE 2.3: a) chematic representation of the target voltage wave form during asymmetric bipolar pulsed sputtering pulse frequency =100 kHz, reverse time 52 ms, duty =80%, and reverse voltage=20% [30] b) chematic representation of reversed voltage pulse-modulation [7]

Using this technique allows the attraction of electrons in the positive pulsed sequence which leads to the neutralization of the positive charge accumulated on the target surface. A schematic representation is given in figure 2.3.

RF deposition

In the RF deposition system the voltage power supply is replaced by a radio-frequency generator. The target is powered by an RF power supply while the chamber is grounded. A typical value of the frequency used is 13.56 MHz. The AC signal causes the electrodes to alternately behave as cathodes and anodes. This makes electron to oscillate between the electrodes causing the ionization of gas molecules. Due to the difference in mass between the electrons and ions, the electrons follow the change in electric field while the ions are hardly affected. This oscillation increases the collision probability between electrons and gas molecule allowing to work at lower pressure. As the target area is much smaller than the grounded anode (the chamber wall), this asymmetric configuration induces negative self-bias on the target. Due to this negative target bias only a small part of the periodic cycle will be positive. The bias is on the order of one half of

the peak-to-peak voltage of the RF power supplied. A schematic of RF sputtering is presented in figure 2.4.

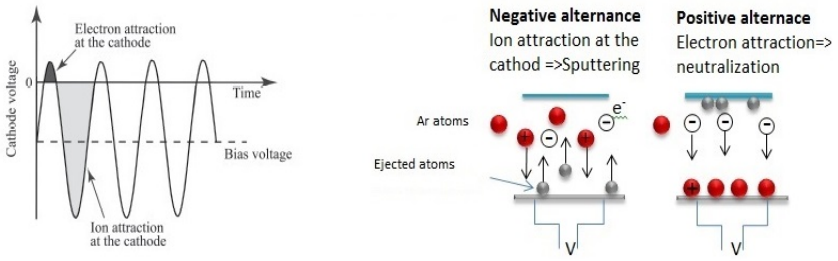

FIGURE 2.4: Schematic representation of the cathode voltage as a function of time. Electrons neutralize the cathode during the positive part of the cycle.

Magnetron Sputtering

The low ionization efficiency encountered in the conventional pulsed DC and RF techniques described before causes the need for high pressure and high discharge voltage. The low generation of ions induces a low deposition rate due to the scattering of the ejected atoms with the gas molecules at high pressure. An alternative solution consists of placing a magnet beneath the target which generate a magnetic field parallel to the surface of the target. This allows to trap the secondary electrons due to the Lorentz force and thus increasing the probability of ionization closed to the surface of the target (see figure 2.5).

A disadvantage of using magnetron sputtering is the erosion profile of the target since the sputtering will be more efficient where the magnetic lines are strong 2.5 . This limits the use of the materials. To over come this problem the used of a rotating magnets [19, 10] or more advanced magnetic design are an alternative solutions.

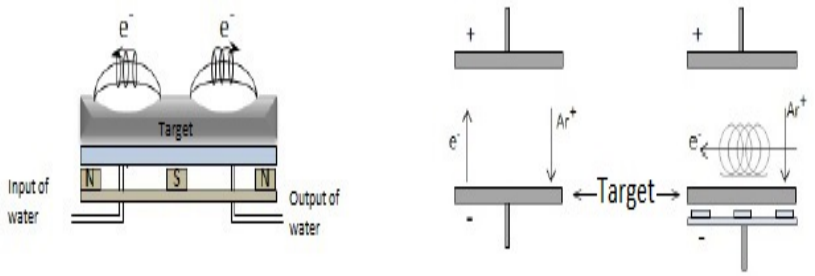

FIGURE 2.5: Schematic representation of the electron confinement in the vicinity of a magnetron.

Reactive magnetron sputtering

Until now we only mentioned the sputtering process using non reactive sputtering gas. The addition of reactive gases in the chamber allows the deposition of several compound material (oxides, nitrides and carbides etc..). The description of the reactive magnetron sputtering was first proposed by Berg [4]. The Berg model is based on gas kinetics balance equation. It takes into account the total rate of the reactive gas, the pumping speed of the gas, the consumption of the reactive gas by the collecting area (A_c namely the chamber wall and substrate) and the target area A_t (see figure 2.6). the balance equations is then written as

$$Q_{tot} = Q_t + Q_c + Q_p \tag{2.4}$$

where Q_{tot} is the total rate of the supply reactive gas , Q_t the rate of the reactive gas consumed by the target, Q_c the rate of the reactive gas consumed by the walls and the substrate and Q_p is the rate of the pumped reactive gas.

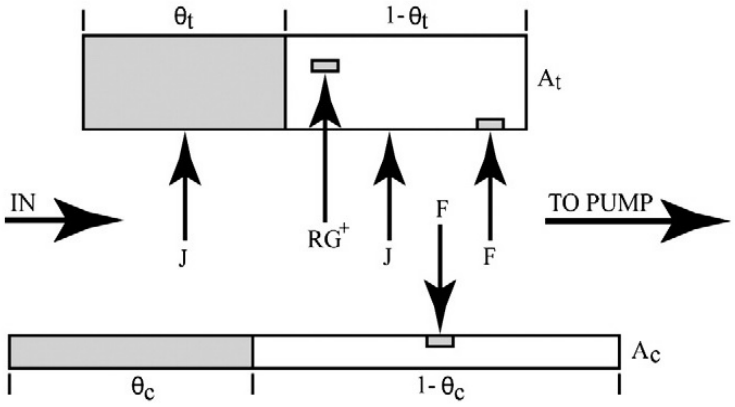

FIGURE 2.6: A schematic diagram of the inside of a process chamber corresponding [3]

The target and the collecting areas consists of two fractions each; pure metal ($1-\theta_t$ and $1-\theta_c$ respectively) and compound (θ_t and θ_c respectively). At the target surface, the amount of the reactive gas consumed is related to the sticking coefficient of the gas on the surface target and it is depending of the nature of the target. When the reaction of the reactive gas occur the metal is converted to compound and added to the compound fraction. The implementation of the reactive gas RG^+ from the plasma and/or knocking-in process from the surface of the compound fraction into the sub-surface of the target will form a compound at the sub-surface of the target. When the sputtering of this compound occurs the ejected compound can be split in metallic atoms and reactive gas atoms. The details of the balance equation formulation can be found in [3][5][4][50].

Here we just want to emphasize that in order to deposited a material with the right composition and controlled structure one should adjust the parameters (gas flow rate, pumping speed, power supply etc..) to be in the sputtering of compound regime. It is clear that the addition of a reactive gas will influence the deposition rate since the sputtering yield of the formed compound (oxide in our case) is usually lower than for the metal. A relation between the deposition rate, partial pressure of the reactive gas, voltage discharge and the supplied flow rate of the reactive gas exist. This relation

induce the so called the hysteresis effect and it is briefly mentioned in the following section

Hysteresis Effect

The introduction of the reactive gases in the chamber cause a competition between the formation of the compound at the surface of the target and the removal of this compound. The hysteresis effect can be describe as follows : at low coverage of the target surface (low pressure) the amount of sputtered metal are larger than the compound formation thus the supplied gas are mainly consumed by the receiving area and the pump. The increase of reactive gas the pressure increase the coverage of the target which results in decreasing the sputtering of the metal atoms. Hence, the consumption of reactive gas is limited by the amount of the available metal atoms at the surface. Therefore the consumption of the reactive gas by the target start from zero , reach a maximum and stays constant since once the rate of the formation of the compound is higher then the sputtering rate the target is fully covered and can not consume the reactive gas any more.The gas consumed by the pump obeys to a linear relation with increasing the pressure. However, the hysteresis effect is a result of the consumption of reactive gas by the receiving areas.

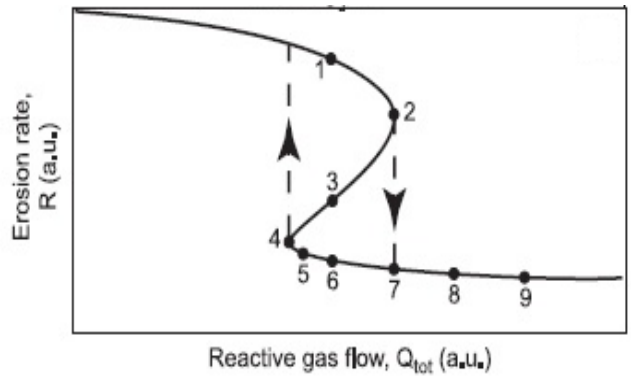

FIGURE 2.7: The normalized erosion rate vs the reactive gas flow [5]

When Q_{tot} is increased the erosion rate decreases until it reaches the position 2. The addition of a small amount of the reactive gas causes the immediate decrease of the erosion from point 2 to 7. This sudden decrease is explained by the fact that for a certain critical value, the target is completely covered which causes the decrease of the erosion rate. Further increase of the reactive gas flow do not influence the erosion rate. The reverse cycle do not follow the same path. As it is shown in figure 2.7 the sudden increase of the erosion rate occurs at a value of the supply gas lower than the position 2. The difference in paths determine the processing region in which the hysteresis effect occurs.

The existence of the hysteresis effect may cause different undesirable effect on the process. The determination of the sputtering regime is required when reactive gases are added.

2.1.2 Film growth

When the atoms are ejected from the surface of the target, they arrive at the substrate with a certain energy. The atoms can migrate from one absorption site to another, re-evaporate or absorbed. The adatoms at the surface start by forming a cluster, then island and finally they coalesce as the film thickness increases. Several parameters influence the growth mode of the thin film. Some are related to the experimental condition such as deposition pressure, substrate temperature and applied power. Others are intrinsic and depend on the nature of deposited material and the nature of the substrate (surface energy , roughness of the substrate and lattice parameter...). The film growth mode can be divided in three modes : 1-Frank-Van der Merwe mode or layer-by-layer mode which takes place when the interaction adatom-substrate are favourable. 2- Volmer-Weber or island growth occur when the interaction between the adatom-adatom are favourable. At the first stage a small distinct clusters are formed by nucleation on the substrate, as this clusters increase there size they form island which grow and coalesce to form the film. 3- The last mode is a hybrid mode which combine the layer-by-layer mode and island mode is named Stranski-Krastnov mode. In this mode at the earliest stage the film is growth as a layer-by-layer, the result of mismatch lattice parameters derive this growth to become an island mode. The three mode are illustrated schematically in the figure 2.8 below.

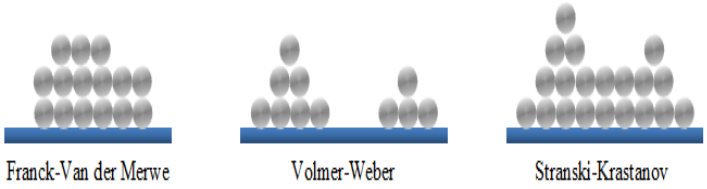

FIGURE 2.8: Schematic representation of the three growth mode

As the film continue to growth, its micro-structure will depend strongly on the mobility of the adatoms. When the mobility of the adatom is high enough a film with large crystals is obtained. The adatoms surface mobility can be increased either by increase of the kinetic energy of the atom ejected from the target (low pressure and high power discharge) or by increasing the substrate temperature. Other parameters such as deposition rate affect the structure of the growth film. For low deposition rate, the adatom arriving at the surface have enough time to diffuse and to find a energetically favourable position on the substrate. However, high deposition rate will cause the adatom to be continuously covered by other adatoms thus limits there surface mobility and increase the stress in the deposited films which might leads to its delamination.

Structure zone model proposed by Movchan et Demenchisin [41] and Thornton [55] gives a complete view of the micro-structural and the morphology of thin film growth as a function of the temperature deposition T and the fusion temperature of the deposited material T_f and the deposition pressure.

Other approaches can be taken to describe the film structure. It is based on the surface energy description. This description is highly useful when the substrate and the deposited film have different chemical nature. A detailed review on the calculation of surface energies is given in [42]. These calculations were made by supposing the drop model which describe the wettability of a metal liquid drop on ZrO_2 substrate. Briefly, the drop model consist of balancing surface energies between a liquid drop

and the substrate as illustrated in figure 2.9. In thermodynamic equilibrium and in the absence of anisotropy of the surface oxide Young's equation is written as :

$$\gamma_{oxide} = \gamma_{metal} \times \cos(\theta) + \gamma_{interface} \tag{2.5}$$

where γ_{oxide} is the surface free energy of the oxide substrate, γ_{metal} is the surface free energy of the metal overlayer, $\gamma_{interface}$ is the interface free energy including any metaloxide interaction, and θ is the contact angle between metal and interface. The surface energy is inaccessible experimentally. However the work adhesion(W_{ad}) can be measured and it is related to the surface energy by :

$$W_{ad} = \gamma_{metal} + \gamma_{oxide} - \gamma_{interface} \tag{2.6}$$

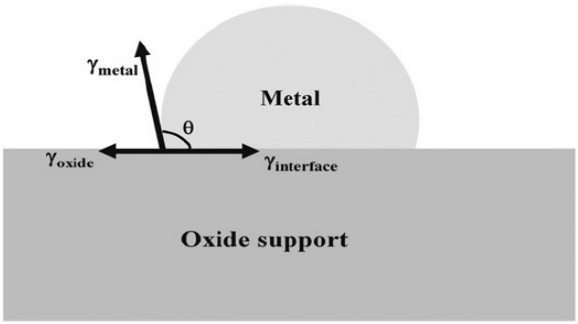

FIGURE 2.9: Schematic of a metal island on a flat oxide support in thermodynamic equilibrium.

The mechanical strength at the interface is closely related to the metal-interface interaction. Moreover, it is clear from equation 2.5 that the interface energy will strongly influences the growth behaviour of metal overlayers. Hence, determining wetting or non-wetting of the metal, layer growth or island growth can be obtained. Several studies has been conducted to determine the surface energies of several metals on $ZrO2$ [12, 33]. The table 2.10 gives some examples of experimental value of the contact angel measure for several metal liquid deposited on $ZrO2$ as given by [42]. In our study as we will see , we deposited Al/W with a composition ratio $\frac{Al}{W} = \frac{1}{9}$. It is acceptable to consider that the addition of small quantity of tungsten will not change the contact angle from the value measured for aluminium (see figure 2.10). Thus for the case of stoichiometric ZrO_2 the growth of Al/W is expected to be columnar. Furthermore, the deposition of a metal on oxide can leads to formation of a mixed interlayer at the interface. Based on the "image charge theory", the charge re-distribution of the metal caused by the contact with an oxide create a potential at the interface given by :

$$V(r,z) = \frac{-q}{\sqrt{r^2 + (z_0 + z)^2}} \tag{2.7}$$

Wettability angles (θ, in °) of different pure metals on stoichiometric (ST) and non-stoichiometric (NST) ZrO_2 monocrystals [219], and on ZrO_2 polycrystals (PL) [218], measured at the melting point of the liquid phases

Melt	θ_{ST}	θ_{NST}	θ_{PL}	γ^e_{LS}	γ^t_{LS}
Al	110				
Si	105		71[a]		
Ti			140[b]		
V	65	60			
Fe	93		116	1.473	1.643
Co	105		123[c], 126	1.719	1.647
Ni	90	85	122[c], 122	1.603	1.624
Cu	147	120	121[c], 125	1.591	1.595
Ge	95				
Rh	105	105			
Pd	98	84			
Ag	148	130	124	1.409	1.595
In	125		153	1.741	1.742
Sn	145	100	170[c], 180	1.805	1.724
Pt	94	80			
Au	125	115			
Pb			155[c], 170	1.629	1.678
Bi			162[c], 180	1.567	1.565

When available [218], the semiempirical and theoretical values of the interfacial energies (respectively γ^e_{LS} and γ^t_{LS}, in J m^{-2}) are also provided.

FIGURE 2.10: Experimental values of the contact angle of different metals on ZrO_2 [42]

where q is the charge of an electron positioning at z_0 and r is the distance parallel to the surface. The image charge theory assume that the interaction between the anion on the oxide and there image at the metal are describe by coulomb interaction (see figure 2.11). These interaction might give an adhesion energy of the order of J/m^2 [13]. Moreover, the polarization effect due to the distortion of the valence band of the metal atoms supported by ionic oxide can increase the adhesion energy at the interface. These effects are to be taking into account when applying plasma cleaning process, because at the interface oxide/metal/plasma and oxide/oxide/plasma the process will not be the same. Even though, Radio-frequency is applied to sputter the film, the charge accumulation will be more pronounced at the oxide/plasma than the metal/plasma interface which enhance the sputtering yield for the latest. However, close to the interface oxide/metal, an electric field can be developed due to the charge image effect which can decrease the sputtering yield at the interface.

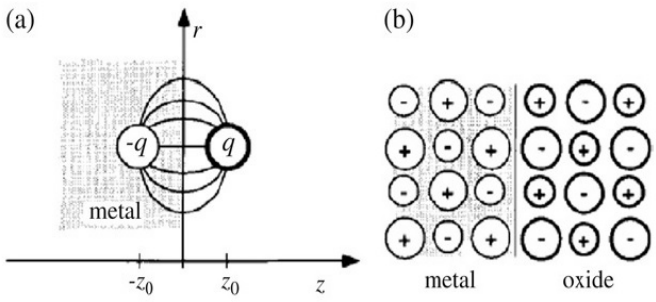

FIGURE 2.11: Charge interaction. (a) Interaction between a point charge q and a metal surface. (b) Image charges at a metal/oxide interface

Chapter 3

Characterization techniques

After having introduced the deposition techniques and film growth theory and the phenomena that might take place at the interface of the deposited films, we shall now give an insight of the characterization techniques used during this project. We will only describe the X-ray photo-electron and ellipsometry spectroscopy in more details, a brief description of UV-Vis measurement is also given. However, other methods such as X-ray diffraction (XRD) , Scanning Electron Microscope (SEM) and Aftomic Force Microscopy are not explained here and but can be found somewhere else [18, 58, 31, 17].

3.1 Introduction to XPS

X-ray photoelectron spectroscopy is a very used technique to study the electronic properties of materials. The most fundamental process of XPS is the photo-electric effect found by Einstein for which he got a nobel price in 1905, that state if a photon with an energy higher or equal to the binding energy of the electron, the ionization effect can takes place:

$$BE = h\nu - KE \tag{3.1}$$

where $h\nu$ is the energy of the incident photon , KE is the kinetic energy of the emitted electron and BE is the binding energy of the ionization potential. The BE energy is taken as the difference between the N electrons of un-ionized state and N-1 electrons in final state (ionized state) so that the BE can be expressed as :

$$BE = E^{N-1}(final) - E^{N}(initial) \tag{3.2}$$

therefore equation (3.1) become :

$$E^{N-1}(final) - E^{N}(initial) = h\nu - KE \tag{3.3}$$

The main quantity measured by XPS is then the KE. The precision of this latest is depend on the the X-ray source, the electron analyzer (which allows the measurement of the kinetic energy of emitted electrons),the detector (which gives information about the number of electrons having a given kinetic energy), and the system commanding the operation of the spectrometer. In the case of metals studied by XPS the work function of the samples and the spectrometer is similar, meaning that the binding energy measured with respect to the fermi level is :

$$BE = h\nu - KE - \Psi_{sp} \tag{3.4}$$

In the case of insulators and semiconductors due to the loss of electrons through emission, the sample become charged which causes a shift of the the effective Fermi energy with respect to the Fermi energy of the spectrometer. That makes the BE hard to determine and other methods can be applied to determine the BE of the elements in the sample by making correction of the energy shift. Other effect occur when solids are to be analysed by XPS is the broadening of the peaks. The peaks can be broadened due to intrinsic and extrinsic factors. The extrinsic factors are a result of the resolution of the electron energy analyzer and from the distribution of the photon flux of the source. In most laboratories Al or Mg K_α are used as photon source. In general laboratories XPS the broadening of the full width at half maximum(FWHM) is about 1eV. While the high XPS resolution at synchrotron have a FHMW of about 0.25 eV. The intrinsic broadening have several origins such as the lifetime of the core-hole state, the inhomogeneity of the material and vibrational broadening etc...

An other powerful feature of XPS is ability to determine the shift in energy due to changing in the chemical environment of the atoms, ΔBE represent the shift in the binding energy of the core level. The shift might be of different origins such as the charge transfer or the binding between elements. The problem with the shift in binding energy determination is that it connect the difference in the initial and final state. This can be solved in the ideal case by supposing that the removal of an electron from an inner shell do not influence the remaining electrons, this approximation is referred to "frozen orbital function" the binding energy is then expressed as :

$$BE_k(initial) = \left\langle \Psi_k^{N-1} \middle| H_k^{N-1} \middle| \Psi_k^{N-1} \right\rangle - \left\langle \Psi^N \middle| H^N \middle| \Psi^N \right\rangle = -\epsilon_k \tag{3.5}$$

where k describe the hole created in the kth shell , Ψ^{N-1} is the wave function of the N-1 electron state and $\Psi^N$is the wave function of the N electron state, H is the Hamiltonian and ϵ_k is the orbital energy. However in solids the relaxation effect of electrons (redistribution of the electrons in the shells) takes place. To account this into a more general formula, once can treat the wave function of N-1 electrons state as a sum expansion of the determinant $\Psi_k^{N-1} = \sum_{k,\alpha} C_{k,\alpha} \Psi_\alpha^{N-1}$. As for the binding energy of the initial state, the binding energy of the relaxed electrons can be writting as ;

$$BE_\alpha = \left\langle \Psi_\alpha^{N-1} \middle| H_\alpha^{N-1} \middle| \Psi_\alpha^{N-1} \right\rangle - \left\langle \Psi^N \middle| H^N \middle| \Psi^N \right\rangle = -\epsilon_R \tag{3.6}$$

where ϵ_R is the relaxation energy. The shift in binding energy is then determined by:

$$\Delta BE = -\Delta\epsilon_k - \Delta\epsilon_R \tag{3.7}$$

then ΔBE is the change in the binding energy, $\Delta\epsilon_k$ and $\Delta\epsilon_R$ is the change in the orbital and relaxation energies respectively. The two contributions (initial state and final state) are impossible to distinguished in XPS measurement for an insulator samples. The use of the auger parameter is very used to solve the charge correction and thus the determination of the the binding energies of the elements.

3.1.1 Auger transition

The ejection of the electron from an inner shell α of energy E_α, leads to an unstable system that tend to minimize it energy and reorganize itself. This can happen through two process : radiative and non-radiative process. The first is a consequence of a transition from an electron of an upper shell β to fill up the hole created in the sub-shell

α, the excess of energy appears as a radiation of a frequency ν. The second process is occurring when the primary hole is filled up with and electron from a level β and the energy gained during this process is taken by an electron in level γ which is emitted as an Auger electron. The ejected Auger electron leaves the atom with a kinetic energy :

$$E(\alpha\beta\gamma) = E_B(\alpha) - E_B(\beta) - E_B(\gamma) \tag{3.8}$$

Depending on how deep is the primary hole is created the intensity of the Auger electron changes.

The auger transition is a consequence of the Coulomb interaction. The description of the transition probability and the line shape of Auger electron is beyond the scope of this report but the reader can refer to [8] for detailed mathematical description of the Auger effect. Here we want to focus on how the combination of the Auger electrons and the binding energies measured with XPS can leads to fundamental understanding of the electronics properties of the deposited films and how the auger parameter can be used to the charge correction of the shifted spectra due to the charging of the sample. We also want to demonstrated that by choosing the appropriate Auger line that is hardly affected by the static charging of the sample can also be a method to correct the shifted spectra.

3.1.2 Auger parameter

When studying insulators or semiconductors, the measurement of the position of the core level binding energy is doubtful. This because of the Fermi level of the insulator and semiconductor are not well define with respect to the Fermi level of spectrometer. Wagner first reported that the position of the kinetic energy of the emitted Auger electron and the core level kinetic energy can be measured with sufficient accuracy in the presence of a static charge. Wagner proposed that the difference in the kinetic energies of prominent and conveniently situated Auger electron and photo-electron peaks compensate each other in the presence of a static charge. The auger parameter is then defined as:

$$\alpha = E(\alpha\beta\gamma) + E_B(\alpha) = 2\epsilon_R \tag{3.9}$$

The measured value of $E(\alpha\beta\gamma)$ and $E_B(\alpha)$ of the same sample under the same measurement conditions are both affected in the same manner by the charging of the sample. Therefore the difference between the two kinetic energies $E_B(\alpha) = h\nu + E(\alpha\beta\gamma)$ cancels out in the present of charging. However, the use of the auger parameter is applied under the assumption that all the auger lines are equally shifted with the change of the chemical environment. This statement reveals to be true for a large class of materials where the relaxation effect are not strong [23]. Therefore an appropriate choice of the Auger transition has to be made. In the case of ZrO_2 as we will see later, the binding energy of the inner shells do not shift equally. A discussion of the use of the auger parameter, carbon C1s reference and the choice of the auger inner shell to correct the charging effect of the sample is given at section 4.1.5 .

3.2 Ellipsometry Spectroscopy

Ellipsometry is a technique based on the measurement of the change in light polarization upon light reflection from a surface. The measured quantity provided by the ellipsometry are : the amplitude ratio ψ and phase difference Δ between light waves.

The measured spectra are then fitted with the desired model depending on the nature of the film. What makes this technique so powerful is the ability of extracting a large amount of information without harming the sample. By constructing the appropriate model ,the optical constant (the complex dielectric constant, the refractive index and the absorption coefficient) , the film thickness and surface roughness can be extracted directly. From the obtained optical constants and film thickness the transmission T and reflection R for different angle can be calculated. Electronic transitions such as interband transitions which gives a direct information about the energy band gap can also be determined using Ellipsometry. Since this later is connected to the surface temperature, alloy composition, grain size and phase structure. These properties can be obtained from analysing the UV/Vis region. The analyse of the infrared region allows the extraction of the carrier concentration, mobility and resistivity of the studied film. Moreover, the vibrational modes and local structures can also be studied. The use of ellipsometry spectroscopy as an in-situ method during film deposition can permit the study of film growth in real time.

3.2.1 Element of theory

When an electromagnetic wave arrive on a surface, one part can be transmit or absorbed while the other part can be reflected.

The polarization of the electric field of the incident wave can be decomposed into two vectors noted E_{is} and E_{ip} for parallel and perpendicular component respectively. For the reflected wave the electrical field can be decomposed also in the same manner E_{rs} and E_{rp}.

The change in the polarization of the electrical field after reflection do not behave in the same manner for the two component. The behaviour of the reflected electrical field is given by Fresnel coefficient defined as :

$$\vec{r_s} = \frac{E_{rs}}{E_{ip}} = |r_s|e^{i\delta_s} \quad ; \quad \vec{r_p} = \frac{E_{rp}}{E_{ip}} = |r_p|e^{i\delta_p} \tag{3.10}$$

The module of the two coefficient $|r_s|$ and $|r_p|$ represent the modification of the amplitude of the electric field , δ_s and δ_p are the difference in phase between the incident and the reflected wave. In ellipsometry measurement these quantities are related to the amplitude ratio ψ and phase difference Δ by :

$$\frac{r_p}{r_s} = \tan(\psi)e^{i\Delta} \tag{3.11}$$

where $\tan(\psi) = \frac{|r_p|}{|r_s|}$ is the ratio of the complex amplitude of the perpendicular and parallel component and $0° < \psi < 90°$ while $\Delta = \delta_p - \delta_s$ is the difference in path caused by the reflection. This is represented in figure 3.1.

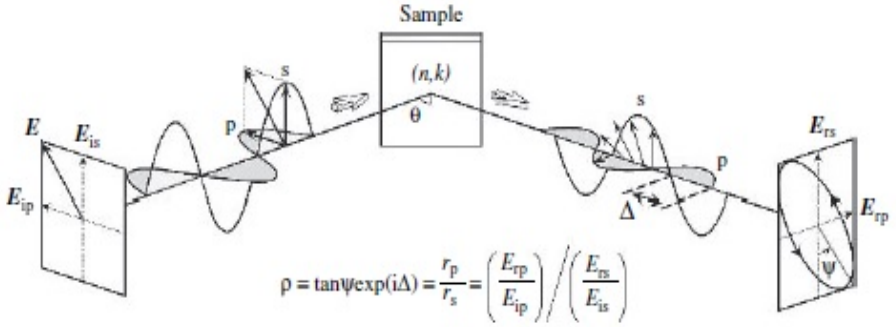

FIGURE 3.1: Characterization of physical properties by spectroscopic ellipsometry.

The measurement error of ψ and Δ strongly depend on the type of spectroscopy. There are different types of configuration of ellipsometry such as RAE (Rotating Analyser Ellipsometry)which is the type of ellipsometer used in this study , Rotating Analyser Ellipsometry with compensator , RCE (Rotating Compensator Ellipsometry), PME (Phase Modulation Ellipsometry) etc.. each type of these ellipsometer have there advantage and inconvenient and depend whether it is used for in-situ real time measurement which require a small measurement time or ex-situ measurement. All the above ellipsometry tend to determine the Stokes parameters. However, Stokes parameters depend on the type of used ellipsometers since these parameters depend on the accuracy of the measurement. The stokes parameters are given by :

$$S_1 = -\cos(2\psi) \quad ; \quad S_2 = \sin(2\psi)\cos(\Delta) \quad ; \quad S_3 = -2\sin(2\psi)\sin(\Delta) \tag{3.12}$$

The minimization of the measured error of ψ and Δ leads to high precision of the thickness and optical properties. The thickness precision for an ellipsometer is obtained by $\delta d = \frac{\lambda}{4\pi n \cos(\theta_i)}\delta\Delta$. For ZrO_2 if we assume that $n = 2.15$ and $\lambda = 6328$. By substituting $\delta\Delta = 0.01$ the precision on the thickness is $\delta d = 3$ which correspond to half lattice parameter of ZrO_2 in cubic phase. However, the determination of the low absorption coefficient using ellipsometry gives rather large error when it is evaluated at low photon energy. This is one of the disadvantage of ellipsometry. To determine low absorption coefficient at low photon energy other methods can be used such as transmittance/reflectance measurement and photo-current measurement.

Fore more informations the reader can refer to [16]. An insight of Tauc-Lorentz (TL) model is given in the following section.

3.2.2 Tauc-Lorentz model for ellipsometry characterization

The used of Tauc-Lorentz model has been widely used in the literature to model the dielectric function of ZrO_2 [22, 66]. It is widely used to study amorphous and poly -crystalline materials. This model is derived from a combined classical system of a dipole oscillation of spring-mass (known as Lorentz oscillator) and Tauc joint density of state. The dielectric functions are expressed as :

$$\epsilon_2(E) = \begin{cases} \frac{AE_0C(E-E_g)^2}{(E^2-E_0^2)+C^2E^2} \cdot \frac{1}{E} & \text{if } E > E_g \\ 0 & \text{if } E \leq E_g \end{cases}$$

and

$$\epsilon_1(E) = \epsilon_1(\infty) + \frac{2P}{\pi}\int_{E_g}^{\infty}\frac{\zeta\epsilon_2(\zeta)}{\zeta^2 - E^2}d\zeta$$

where for the imaginary part of the complex dielectric function , A and C represent the amplitude and broadening of the ϵ_2 peak which include the optical transition element matrix. While E_0 and E_g represent the peak in the joint density of state and the gap energy respectively. For the real part of the complex dielectric functions is obtained by performing a Kramers Kronig integration of ϵ_2 , P is refereed to Cauchy principal part. The detailed expression of $\epsilon_1(E)$ is given elsewhere [27].

One should keep in mind that Tauc-Lorentz is an empirical model and does only account for interband transitions. These transitions are useful to determine the optical band gap of the material under consideration and is determined under the assumption of a parabolic band by :

$$[\alpha(\nu)\cdot h\nu]^{\frac{1}{2}} = const\cdot(h\nu - E_g) \tag{3.13}$$

where $\alpha(\nu) = \frac{4\pi}{\lambda}\cdot k(\nu)$. The optical band gap is obtained by extrapolating the linear portion of the plotted curve from equation (3.13).

The measured ψ and Δ for different angles ($45° < \theta < 70°$) are fitted by the constructed model using an iterative method. The best fit is obtained by minimizing the error function between the experimental and modelled spectra (see figure 3.2) . The error function is defined as :

$$\chi^2 = \min\sum_{i=1}^{n}\left[\frac{(\psi_{Model} - \psi_{Exp})^2}{\Gamma_\psi}i + \frac{(\Delta_{Model} - \Delta_{Exp})^2}{\Gamma_{Delta}}i\right] \tag{3.14}$$

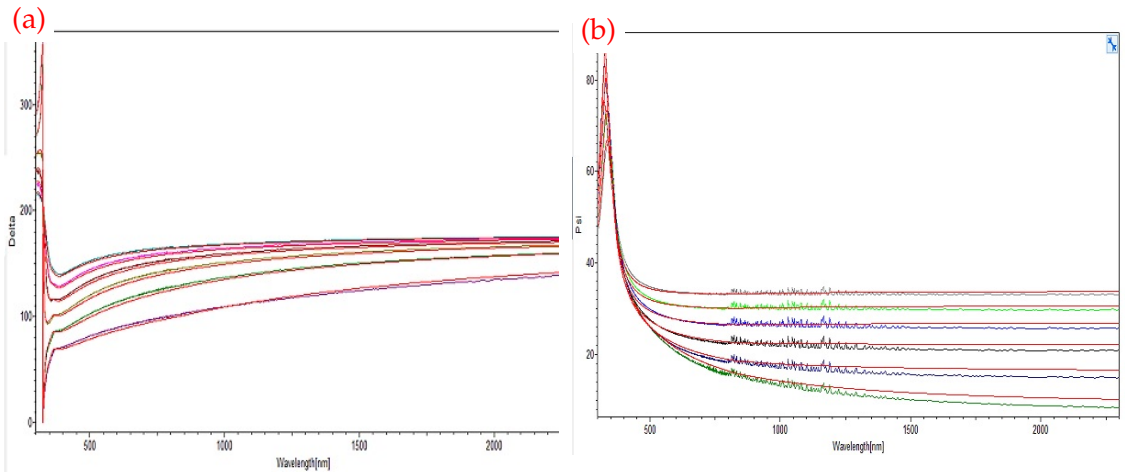

FIGURE 3.2: The best fit obtained from experimental (color lines) and theoretical model (black lines) using TL for a) Δ b) ψ of ZrO_2 obtained in this study

3.3 Spectrophotometry UV-Vis for optical characterization

The use of UV-Vis measurement is complementary to ellipsometry measurement. Because the UV-Vis technique allows the direct measurement of the transmittance (T) and the reflection (R) of the film, this measurement can be compared to the simulated T and R obtained from TL model. As we mentioned before the TL model take into consideration only the inter-band transition. However, in solid state due to the imperfection of the lattice structure of the film and the existence of several impurities causes the formation of defect states that act like trapping centre, several other transitions can occur. The use of UV-measurement allows the measurement not only the inter-band transitions but also intra-band transitions. This transitions are represented schematically in figure 3.3. Because of the the interaction of the excited electron with hole, the optical transition can generate an exciton (electron hole pair) with an energy lower than the band gap. More details can be found in [51].

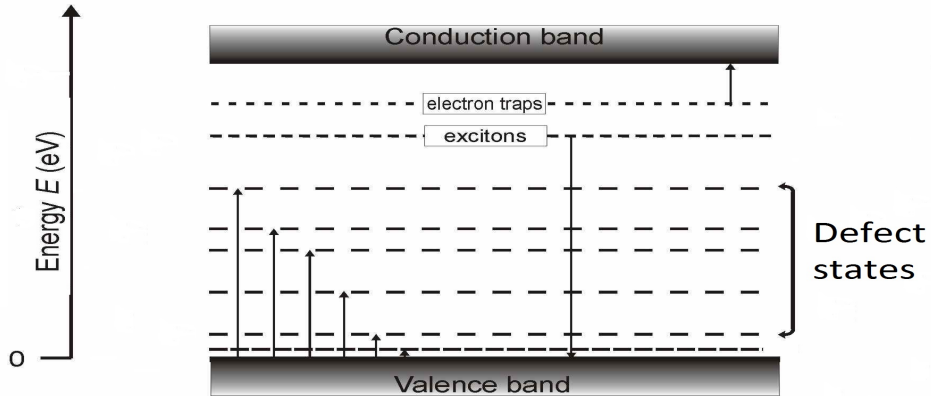

FIGURE 3.3: Schematic representation of different electronic transitions.

Chapter 4

Results and discussion

4.1 Experimental conditions for thin films deposition

This section will be dedicate to procedure and conditions used for several films deposition. Pulsed DC magnetron sputtering was used to deposit Al/W, Al and Rh, while RF and pulsed DC reactive magnetron sputtering were used to deposit ZrO_2 films. The base pressure before deposition was kept at $P_{initial} = 3 \times 10^{-8} mbar$ for Al/W,Al and Rh to obtain oxygen free film. All films were deposited on Silicon (100) one side polished and Ar was used as a sputtering gas. For pulsed DC ZrO_2 deposition the initial partial pressure was $P_{initial} = 2 \times 10^{-7} mbar$ and for RF deposited film an initial partial pressure was kept at $P_{initial} = 3 \times 10^{-8} mbar$. In both cases a mixture of Ar and O_2 were used. For all films deposition the target was cleaned using Ar plasma in order to remove any absorbed oxygen at the surface. For the reactive magnetron deposition, a plasma homogenization were performed for all the films. The growth rate was estimated using Quartz Micro-Balance (QMB) and cross checked with SEM cross section. In the case of ZrO_2 films the thickness of the films were measured using ellipsometry spectroscopy and compared to SEM cross section. Furthermore, the core-level of the deposited elements were analysed insitu by X-ray Photo-electron Spectroscopy (XPS) using an MgK_α Radiation source (1253.6 eV). A survey was recorded on each film over the binding energy range from 1070 to -10 eV with a step size of 0.5 eV at a constant pass energy of 48.9 eV. The detected elements were then recorded over the binding energy with a step size of 0.05 eV and a pass energy of 29.1 eV. The obtained spectra were fitted using Unfit 2014 software package.

4.1.1 Deposition of aluminium tungsten

A target of Al/W with composition of Al(90%) and W(10%) was used. The deposition condition is given in table 4.1. The input parameters for QMB are those of the density of Al since we assumed that the low concentration of W will not deviate the thickness estimation from QMB. The SEM top view and cross section are presented in figure 4.1. From this image we can see that the surface is very smooth suggesting an amorphous film. The thickness determination from SEM cross section was measured using Image-J software package [48]. The obtained real thickness was found to be 50nm. This verification allowed us to determine a tooling factor of 0.5 between the real thickness and the input thickness for the QMB. The Growth rate is estimated to be 2.6 Å $/s$.

TABLE 4.1: Deposition condition of Al/W

Method	Deposition pressure [mbar]	Ar flow [sccm]	Power [W]	Frequency[KHz]	Pulse-on [ns]
Pulsed DC	3×10^{-3}	40	40	50	496

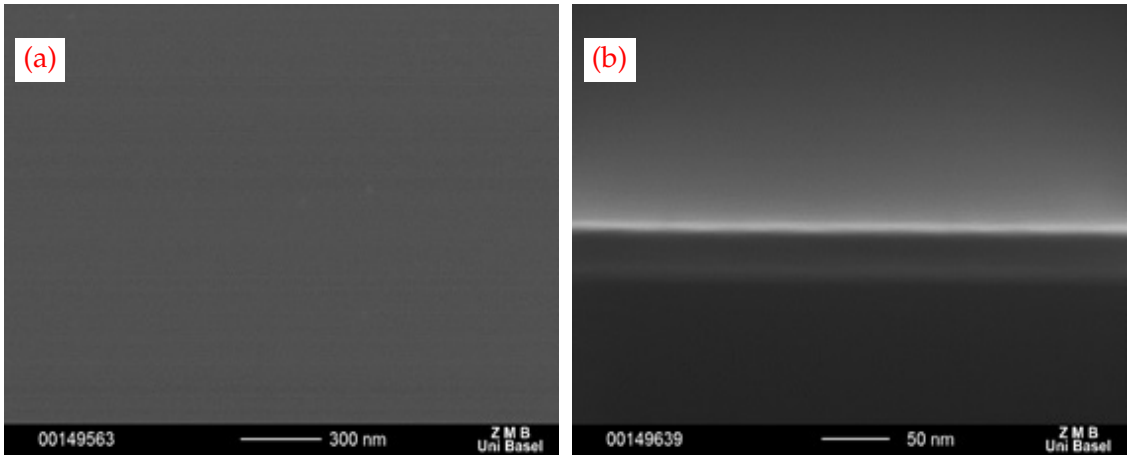

FIGURE 4.1: a)SEM top view b) SEM cross section of Al/W deposited film

The recorded W4f and Al2p core-levels are presented in figure 4.2a. From XPS fitted spectra, $W4f_{7/2}$ and $W4f_{5/2}$ core-level were observed at a binding energy of 30.67 eV and 32.81 eV respectively with a spin-orbit splitting of 2.13 eV . From the literature values , the metallic binding of $W4f_{7/2}$ core-level of tungsten is located at 31.3 eV [60]. This shows that in the present case, the tungsten in metallic state is bounded to aluminium which cause the slight shift toward lower binding energy (see figure 4.2a). The FWHM for $W4f_{7/2}$ and $W4f_{5/2}$ are 0.8 and 0.9 eV. The ratio of $W4f$ peak intensities $\frac{I_{W4f_{5/2}}}{I_{W4f_{7/2}}} = 0.76$ while the ratio of the $W5p_{3/2}$ to the main peak $W4f_{7/2}$ is $\frac{I_{W5p_{3/2}}}{I_{W4f_{7/2}}} = 0.03$. The de-convoluted $Al2p$ spectra shows two main peaks located at 72.65 and 75.16eV for metallic and oxide state respectively . The metallic $Al2p$ is usually located at 72.8 eV. The shifted value observed with respect to the binding energy of metallic $Al2p$ (see figure 4.4) confirm that Al and W are bound. A third peak was added to the fitting of Al2p spectra, it describes the overlap of Al2p peak and W5s (see figure 4.2b). The O1s peak was fitted with two component. The first one have a strong intensity centred at 532.05 eV can be attributed to $Al-O-H$ hydroxyl groups [25], while the peak at 533.87 eV is assigned to adsorbed water molecules [49]. The detail of the binding energy and concentration of all the elements are presented in table 4.2:

TABLE 4.2: XPS binding energies and atomic concentration of Al2p, W4f , W5s , W5p and O1s

	Al metal	Al_xO_y	W metal	$W5s$	$W5p_{3/2}$	Oxygen OH	Oxygen H_2O
BE [eV]	72.65	75.16	30.76	74.11	36.52	532.05	533.87
Concentration [%]	76.6	4.9	8.3	2	0.1	9.6	5.2

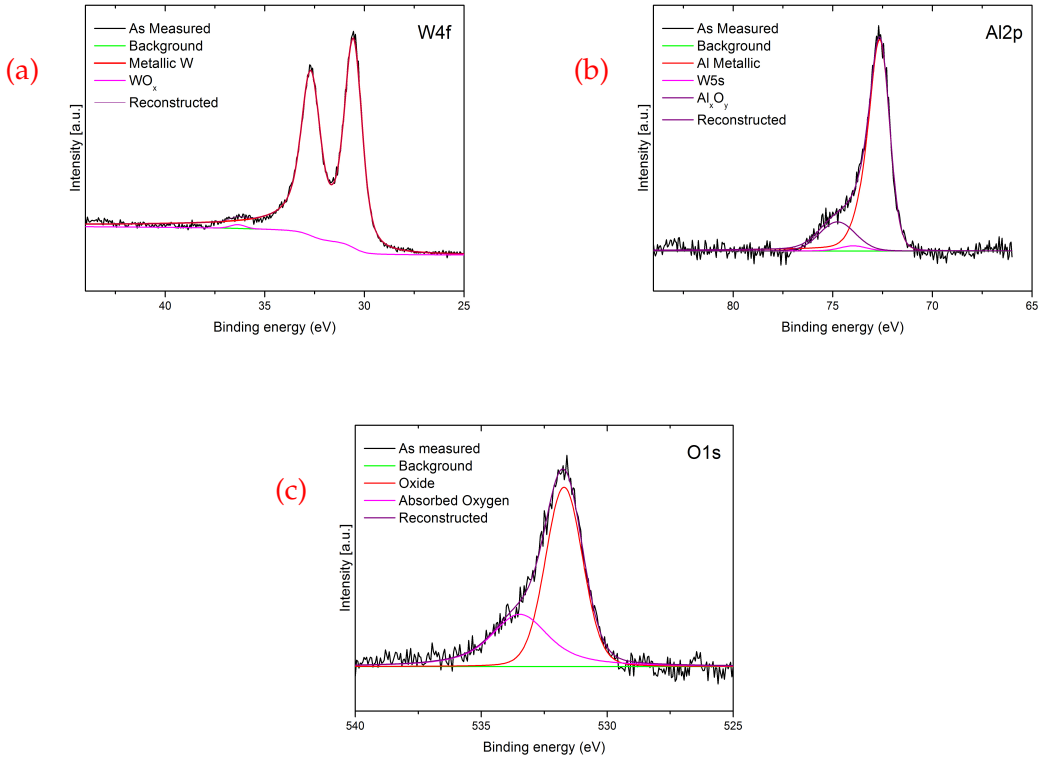

FIGURE 4.2: Core level Spectra for a)W4f b) Al2p c) O1s for the Al/W deposited film

4.1.2 Deposition of aluminium

Aluminium thin film was deposited using pulsed DC magnetron sputtering using 99.99% pure aluminium target. To deposit Al on Si(100) substrate the given experimental conditions in table 4.3 were used. The growth rate of the deposited film under these conditions is evaluated to be 7.2 Å/s.

Method	Deposition pressure [mbar]	Ar flow [sccm]	Power [W]	Frequency[KHz]	Pulse-on [ns]
Pulsed DC	3×10^{-2}	40	97	50	496

TABLE 4.3: Deposition condition of Al

The obtained structure from SEM are presented in figure 4.3 . From top view image we can clearly see the existence of large platelets randomly oriented. This might suggest the existence of crystallite at the surface. Furthermore the cross section image do not reveal any sign of columnar growth suggesting a large wetting angle at the initial stage of growth. Since the deposition was performed at room temperature and relatively high growth rate the formed nuclei do not have sufficient energy nor time to move on the surface of the substrate making a large island formation. Once the island start to coalesce after a certain time , the formation of relatively large platelets starts to occur.

The XPS spectra in figure 4.4, shows a week trace of oxygen . The binding energy of metallic Al is observed at 72.72 eV in agreement with the literature values while the low

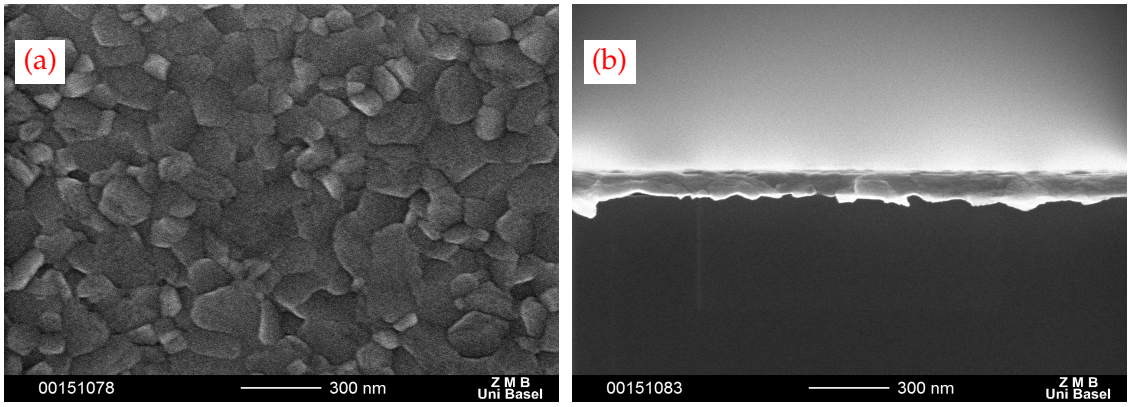

FIGURE 4.3: a)SEM top view b) SEM cross section of Al deposited film

intensity peak centred at 74.47 eV is attributed to Al sub-oxide. The atomic percentage of oxygen is determined to be less then 1%. This prove that a high purity metallic Al can be deposited with the experimental setup available in our laboratory.

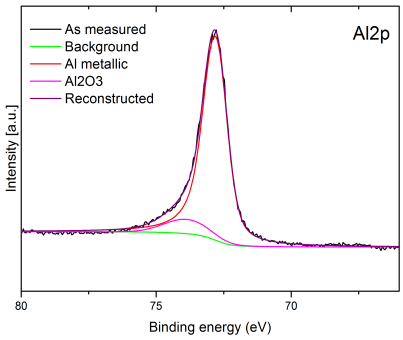

FIGURE 4.4: Core level Spectra for Al2p of Al nearly free from oxygen

4.1.3 Deposition of Rhodium

Rhodium thin films were deposited using both RF and pulsed DC deposition. Ar was used as a sputtering gas . The experimental condition used are given in table 4.4. The parameters were set in a way that the growth rate are equal. The growth rate is determined to be $G_R = 3.1$ Å$/s$. The SEM top view of both deposits are shown in figure 4.5. From SEM images we can clearly see that the film deposited using RF excitation have large and packed grain when it is compared to pulsed DC. The origin of the difference in the morphology are presently not known.

TABLE 4.4: Deposition condition of Rh films

Method	Deposition pressure [mbar]	Ar flow [sccm]	Power [W]	Frequency[KHz]	Pulse-on [ns]
Pulsed DC	6×10^{-3}	40	40	50	496
Method	**Deposition pressure [mbar]**	**Ar flow [sccm]**	**Power [W]**	**Frequency [MHz]**	**DC-Bias [V]**
RF	3×10^{-2}	40	54	13.56	242

Moreover, we observed that the film deposited using pulsed DC technique was completely de-laminated after a few hours the film was deposited, suggesting that the film was subject of high compressive stress resulting in telephone cord phenomena [28]. On contrary the metallic film deposited using RF technique showed no trace of de-lamination.

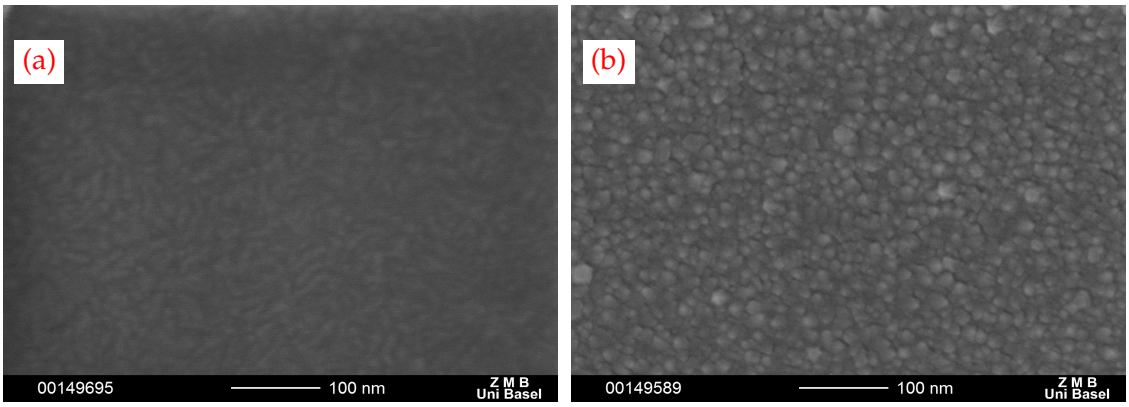

FIGURE 4.5: Top view SEM images of a) Pulsed DC b) RF deposited Rhodium film

In figure 4.6b) a SEM cross section image of RF deposited film shows a well defined columnar growth. We see at the surface of the film a highly faced surfaces with a pyramidal shape. The growth mechanism of the deposited film can be divided into two stages. At the first stage, the adatoms have a high surface energy leading to a redistribution of the arrival flux which cancels the dependence on the condensation coefficient. After a certain time and due to the formation of crystallite with different orientations and condensation coefficients, the diffusion of the adatoms at the surface tend to zero and as a consequence the nuclei start to have a facet shapes. The arriving atoms grow on the existed faceted leading to isolated crystals with sharp features [54].

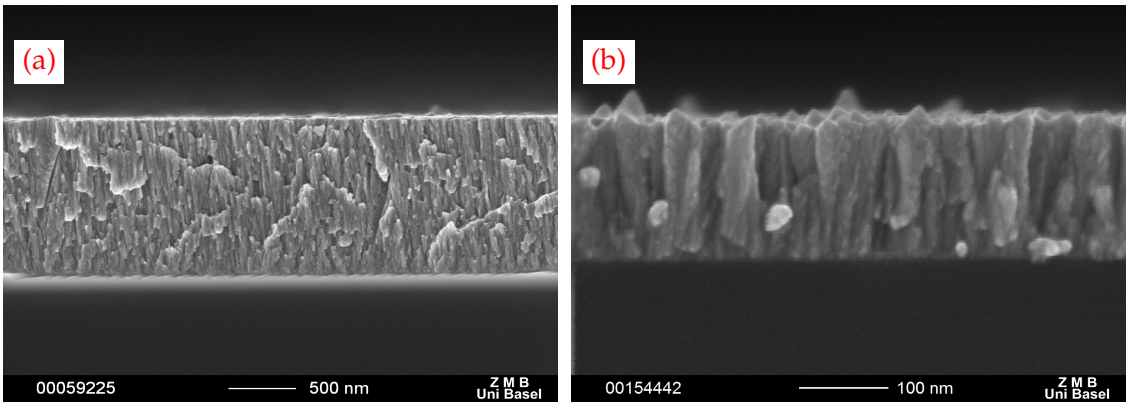

FIGURE 4.6: SEM images of a) pulsed DC [35] b) Cross section from RF deposited Rhodium film

XRD measurement revealed that the formed crystallite has a cubic phase a preferential orientation along (111) direction. The crystalline size determined by the Scherrer formula [44] gives a crystallite size of about 8 nm. The columnar width of the film was estimated from the SEM cross section and it is found to be around 30 nm. The obtained values are in the range of the one reported in [35] (see figure 4.6a) using pulsed DC

magnetron sputtering. However, the obtained columns here are more defined and another interesting features is the appearance of the Rh(222) at 89.14° that appeared only for high substrate temperature deposition (550 $°C$) [35].

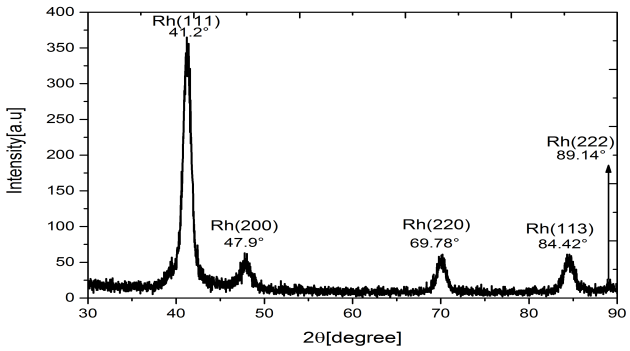

FIGURE 4.7: X-ray diffraction patterns of rhodium films deposited on silicon using RF magnetron sputtering at room temperature

4.1.4 Comparative study of structural and optical properties of zirconium dioxide on Si (100) deposited by DC and RF reactive magnetron sputtering

In this section we discuss the results obtained from the pulsed DC and RF deposition of zirconium dioxide using a metallic zirconium target and a mixture of argon and oxygen . The argon pressure and the power were fixed to 7×10^{-3} mbar and 100 W respectively, while the oxygen percentage defined as $O_2\% = \frac{P_{O2}}{P_{TOT}}$ was varied from 0% to 20% by controlling the flow rate of oxygen via a mass flow controller. Where $P_{TOT} = P_{Ar} + P_{O2}$ and P_{Ar} and P_{O2} are measured individually by introducing only Ar and O_2 respectively. The oxygen pressure was measured during deposition using Zirox Vacuum Probe to determine the amount of the consumed oxygen .

Determination of the sputtering regime

In order to deposit ZrO_2 with the desirable stoichiometry one have to determine the hysteresis cycle which describe the competition between the formation of a compound on the target due to the reaction of the added gas and the sputtering of this same compound. Usually the sputtering yield of oxides is lower than the elemental metallic target which causes a decrease in the growth rate. In the figure 4.8 a plot of the change in the cathode voltage, the growth rate and the oxygen partial pressure as a function of the supplied reactive gas is presented for two different techniques. The obtained curves exhibits three main regions. For the DC pulsed deposition, the first regime correspond to the metallic mode where with increasing the oxygen percentage from 0 to 1 sccm , the discharge voltage, the growth rate and oxygen partial pressure are constant. Increasing the oxygen percentage up to 4.5 sccm causes a decrease of the growth rate due to the competition between the oxidation of the target and the removal of the oxide formed , in the same time the discharge voltage tend to increase from 227 V to reach a plateau of 371 V, this describes the sputtering regime. The latest stays constant as the supplied oxygen is increase further more which describe the oxide regime.

The oxygen partial pressure start to increase linearly suggesting that added oxygen is only consumed by the pupmp and that the target is fully oxidized. The reverse cycle shows a different trend. Down from 5.5 to 4.5 sccm the deposition rate and the supply voltage are constant, decreasing in advantage the supplied oxygen in the chamber the discharge voltage and the partial pressure are higher than the ones obtained while increasing the oxygen percentage. By the time when the oxygen percentage is again 1 sccm we notice a transition from the sputtering regime to the metallic regime where the values of the discharge voltage, the growth rate and the partial pressure reached their initial values. This difference in path between increasing and decreasing the supply oxygen flow describe a hysteresis cycle, where the formation of the ZrO_x is obtained in the sputtering regime for an oxygen flow values between 1.2 and 4.5 sccm. For the RF deposition , the difference in path is barely distinguishable. A difference between the two process is the inverse behaviour of the target discharge voltage. In the case of pulsed DC deposition the voltage at the target tends to increase, while for the case of RF deposition we noticed a decrease of the voltage. The reason behind this difference in voltage behaviours is currently unknown. We would like to draw your attention to the fact that the change from sputtering regime to oxide regime is not accompanied with a sudden decrease of the growth rate nor a sudden decease of the discharge voltage as it is shown in [1]. These differences are explained by high pump speed that is used in our experiment where a turbomelecular pump with a pumping speed of 1500l/s is used instead of 380l/s in [1]. A high pumping speed leads to reduce the hysteresis effect and thus a more stable process [53],[50]. Furthermore, the injection point of the gases in our setup is closer to the pump then to the target which means that the majority of the reactive gas is pumped and that a concentration gradient is created between the pump and the target tend to eliminate the hysteresis cycle [9]

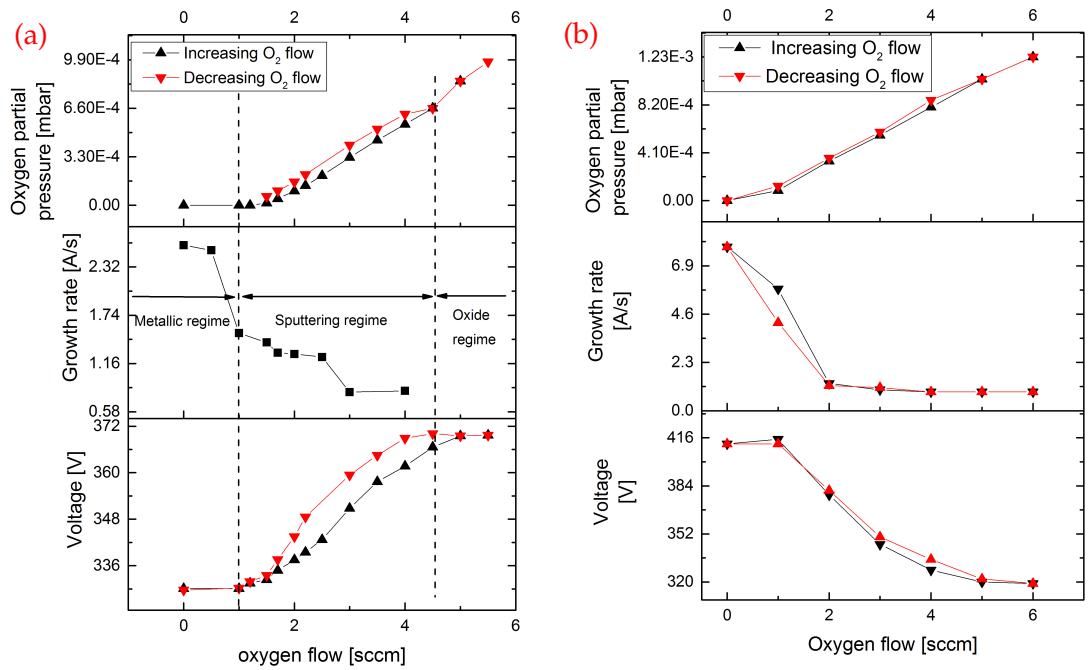

FIGURE 4.8: Cathode voltage , growth rate and oxygen partial pressure as a function of the oxygen flow for a) deposition using pulsed DC magnetron sputtering and b) deposition using RF magnetron sputtering

Structural analyse of ZrO_x

After having determined the sputtering regime, different films have been deposited for different oxygen partial pressure using both pulsed DC and RF reactive magnetron sputtering. The thickness of the deposited film using RF techniques was determined to be 34 nm while the films deposited using pulsed DC have thickness range of 84± 15 nm. It is assumed that the variation of thickness at this range do not influence the crystallite size nor the crystalline phase. The XRD patterns for both deposited films are presented in figure 4.9. We noticed that while RF deposition technique gives a monoclinic (-111) oriented crystallites independently of the the oxygen percentage in the chamber, the DC deposited films shows different features. The increase of the oxygen percentage leads to the change of the crystallite direction. For low oxygen percentage (0 and 2.78%) the monoclinic (200) is dominant. The increase of the oxygen percentage to 9.09% causes the transition from m(200) to m(-111) phase. Further increase of the oxygen percentage causes the appearance of different crystalline directions with a dominant tetragonal t(101) phase.

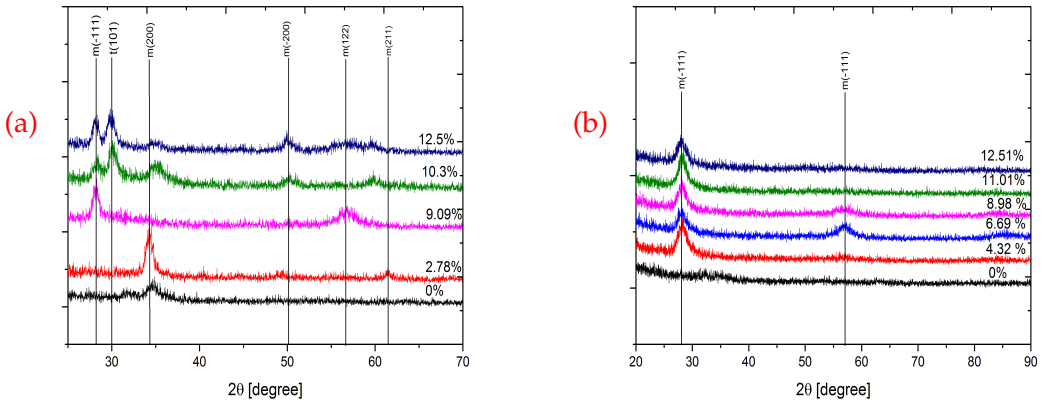

FIGURE 4.9: XRD patterns of a) deposited films using DC Pulsed magnetron sputtering and b) Deposited films using RF magnetron sputtering

By fitting the strongest peaks, the full width at half maximum (FWHM) is obtained. The crystallite size is then calculated using Debby Scherrer formula [44] :

$$D = \frac{0.9\lambda}{B_{1/2}\cos(\theta)} \tag{4.1}$$

Where λ is the X-ray wavelength, θ is the Bragg diffraction angle and $B_{1/2}$ is the full width at half maximum (FWHM)

Figure 4.10 illustrate the variation of the crystalline size as a function of the oxygen pressure. The RF deposited films show a small crystallite size when is compared to DC films. The increase of the oxygen percentage in the chamber causes the increase of the crystallite size to a maximum value of 4.7 nm with conserving the same crystalline direction in the case of RF deposition. An approximate linear behaviour is observed for the crystallite size with respect to oxygen percentage. For pulsed DC deposited film the size of the crystallite is relatively higher than for RF deposited films.

SEM cross section were performed on the pulsed DC deposited films and are shown in figure 4.11. We can clearly see the effect of increasing the oxygen pressure on the film growth. Increasing the oxygen percentage in the chamber allows a transition from

a poorly polycrystalline film (see figure 4.11a,4.11b) to a highly multi-crystalline film (figure 4.11c,4.11d)). The trend of the change in the morphology shown in SEM cross section images is fully supported by the XRD results.

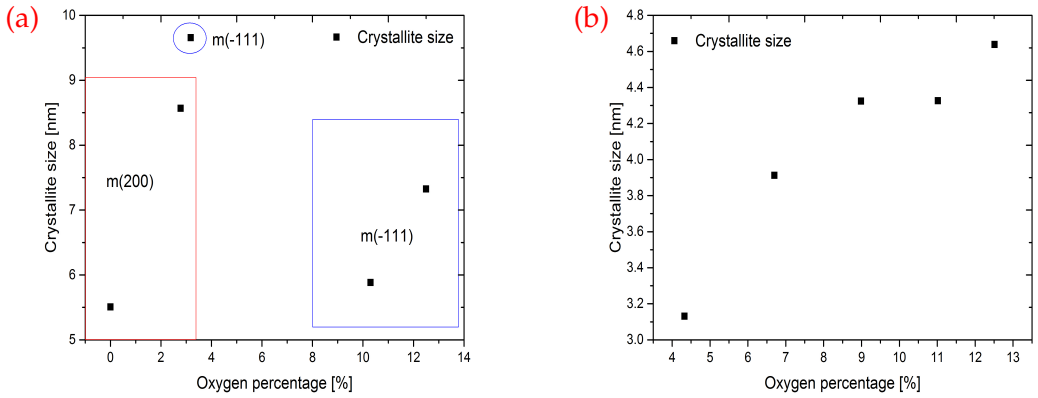

FIGURE 4.10: Variation of the crystallite size as a function of the oxygen percentage in the chamber for a) pulsed DC b)RF deposited film

Moreover, the films deposited at a high oxygen percentage show a columnar growth. The results obtained are in agreement with [64] who suggests that the growth of ZrO_2 on SiO_2 substrate shows a columnar growth at the early stage. For RF deposited film of 34 nm it was not possible to observe any structure with SEM due to the high charging of the sample. To gain informations about the growth of ZrO_2 using RF a thick film of 80 nm was deposited for two different oxygen percentages. By analysing these films the same columnar structure was observed for both low oxygen percentage (4.32%) and high oxygen percentage (11.01%). The XRD measurement on thick ZrO_2 deposited using RF showed no difference with respect to the films of 34 nm. Thus, the SEM cross section (see figure 4.12) shows again a self-consistent results with XRD measurement.

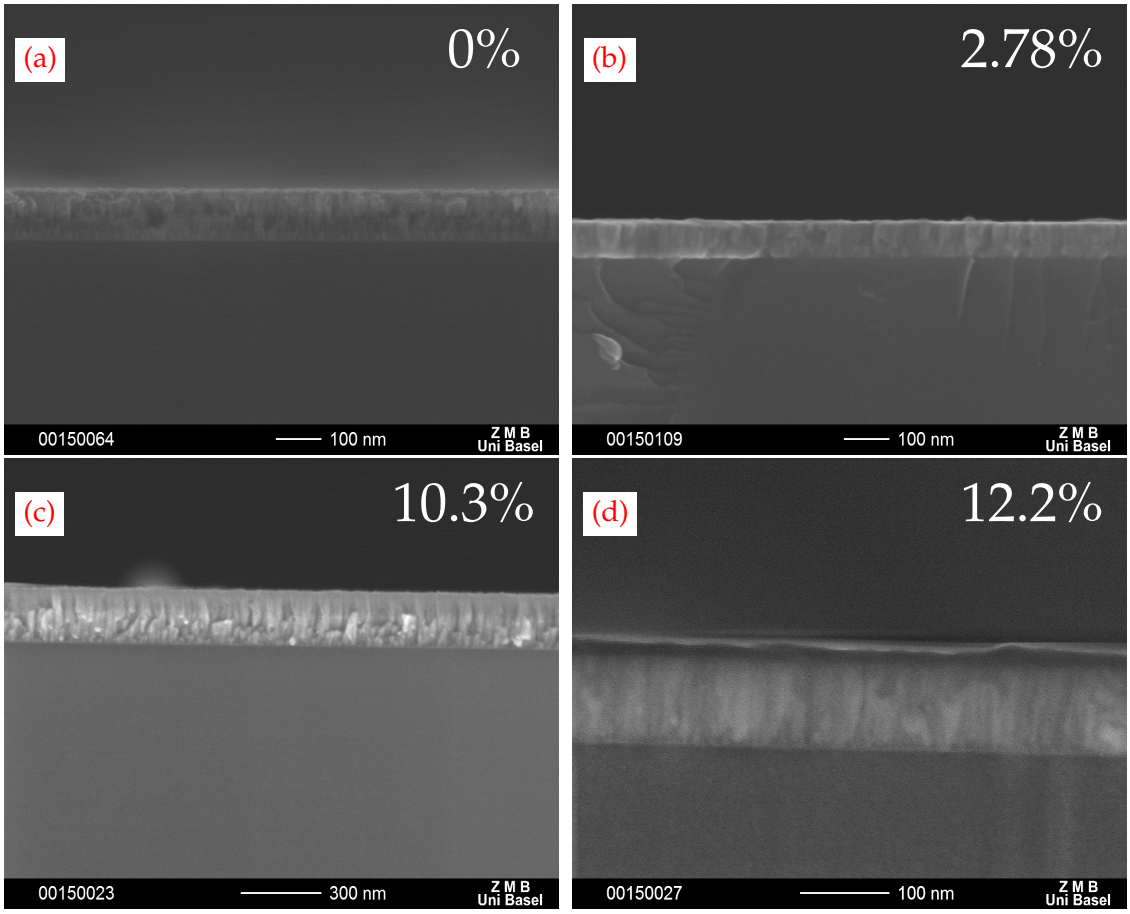

FIGURE 4.11: Evolution of the morphology as a function of the oxygen percentage in the chamber for pulsed DC deposited film

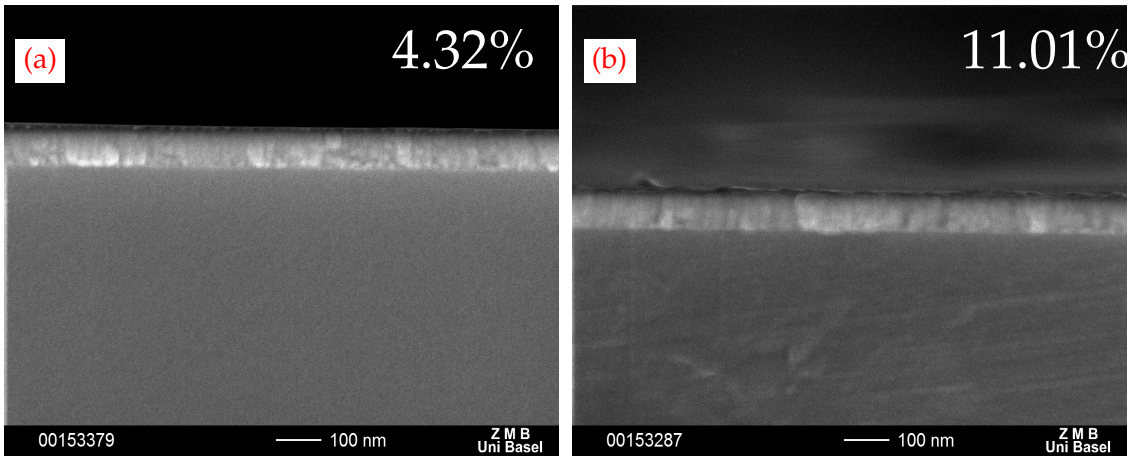

FIGURE 4.12: SEM cross section of RF deposited films of 80 nm thickness for a) low oxygen and b) high oxygen percentage in the chamber

The film roughness was measured using AFM tapping mode. The figure 4.13 shows the change in the surface morphology for pulsed DC deposited films. We notice that the increase of the oxygen percentage does induce a change in the film morphology. However the measured RMS shows that the films stay relatively smooth with a maximum RMS of 1.25 nm recorded for the film deposited at 10.3 % of oxygen in the chamber. Different size area $1\times$ 1 μ , $2\times$ 2μ and $5\times$ 5μ) and different spots of the samples were recorded for each film, showing no difference in the measured RMS: the deposited films have a uniform roughness over the whole surface.

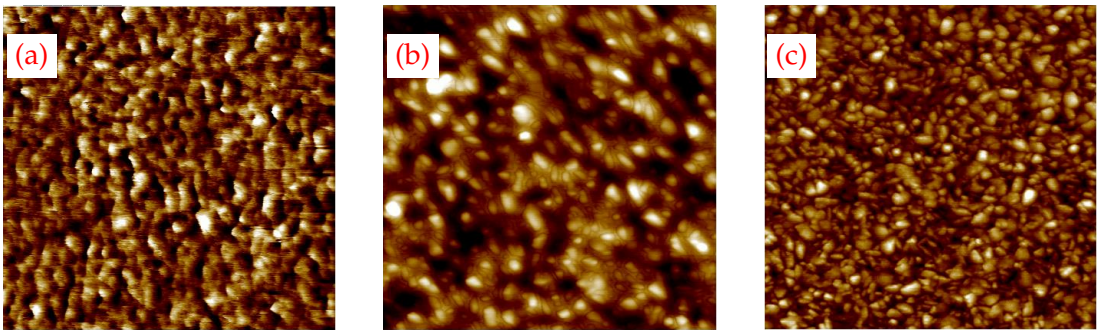

FIGURE 4.13: Evolution of the morphology of pulsed DC deposited films for a) 3.17 b)10.3 and c) 12% of oxygen in chamber. The image size is 500 $\times$ 500 nm with $\Delta Z = 8.7 \quad nm$

The films deposited using RF showed a higher RMS. At low oxygen percentage the films show a large grains (see figure4.14a) when it is compared with pulsed DC deposited one (see figure 4.13a). The increase of oxygen percentage make the grains more compact and increases their density. Moreover, the measured RMS tend to increase with increased oxygen percentage, a maximum value of 2.5 nm was obtained for the film deposited at 9.09 %.

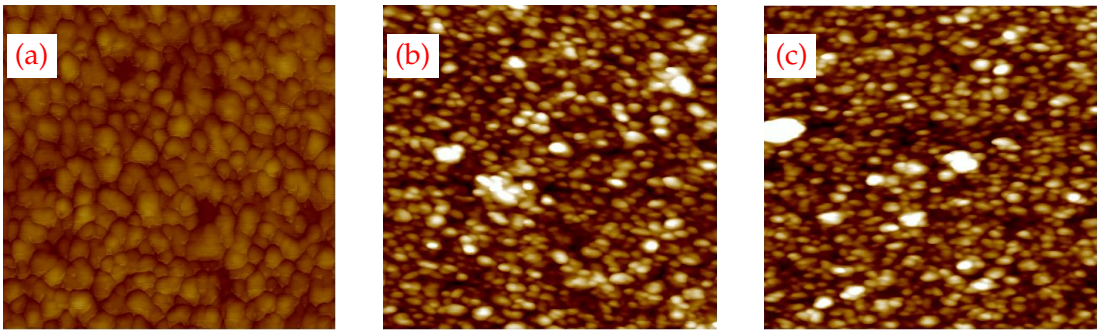

FIGURE 4.14: Evolution of the morphology of RF deposited films for a) 4.32 b) 8.98 and c) 11.01% oxygen in chamber. The image size is 500 $\times$ 500 nm with $\Delta Z = 20nm$

Figure 4.15 summaries the change in the roughness with increasing oxygen percentage. The Zr metallic film deposited using RF shows a very low RMS value (0.28 nm) while the metallic film deposited using pulsed DC have an RMS of 1.15 nm. This difference in film roughness is due to the crystalline structure of the film. The lowest value suggest an amorphous film, while the highest value suggest the existence of certain crystallites at the surface [**pleschinger**]. This assumption is supported by the XRD results (see figure 4.9). The increase of oxygen percentage for RF deposited films

tend to increase the RMS value to a maximum but further increase of oxygen percentage showed that the RMS value decrease slightly. However, for pulsed DC deposited film, at lower oxygen percentage the RMS decrease and reach a kind of plateau of 0.25 nm. A sudden increase is recorded at 10.3 % oxygen where a RMS value of 1.25 nm is obtained. The further increase of the oxygen percentage tend to decrease again the roughness.

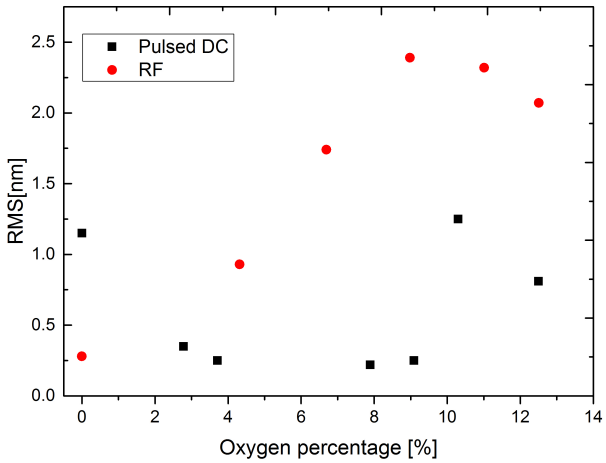

FIGURE 4.15: Variation of the roughness with respect to oxygen percentage in the chamber for pulsed DC and RF deposited film

Optical properties of ZrO2

Both RF and pulsed DC deposited films were characterized using SE, where the measured spectra Ψ and Δ were fitted using Tauc-Lorentz dielectric function (see section 3.2.2). The constructed model consist of four layer. The bare Si(100) substrate was first measured and modelled using Si(100) from the material library and a native oxide of 2.61 nm was added on the top using Cauchy dielectric function . After ZrO_2 was deposited, two layers were added. The first describes the ZrO_2 using Tauc-Lorentz function while the other describes the roughness. This later was constructed using Bruggeman effective medium approximation and a mix of void and ZrO_2 with a fraction of 50%. Figure 3.2 shows the best fits of the measured spectra of the film deposited using RF reactive magnetron sputtering at the oxygen percentage of 11%. The other fits are not shown here. From the obtained fit parameters the thickness, roughness and the modelled reflectivity were cross checked with SEM cross section ,AFM and the measured reflectivity using spectrophotometry UV-Vis. Figure 4.16 shows that the measured and the modelled roughness /thickness are in perfect agreement, with standard deviation of 0.22% and 0.3 % obtained for the roughness and the thickness respectively.

To further validate the constructed Tauc-Lorentz function, the obtained optical constant were used to simulate the total reflectivity of a ZrO_2 on Si(100) a using SpectraRay3 software package. The modelled reflectivity was then compared to the measured reflectivity for wavelength range of 300 to 1040 nm. Figure 4.17a shows that the modelled and the measured reflectivity are in good agreement. Thus the fitted Tauc-Lorentz parameters are a good description of the optical properties of the deposited

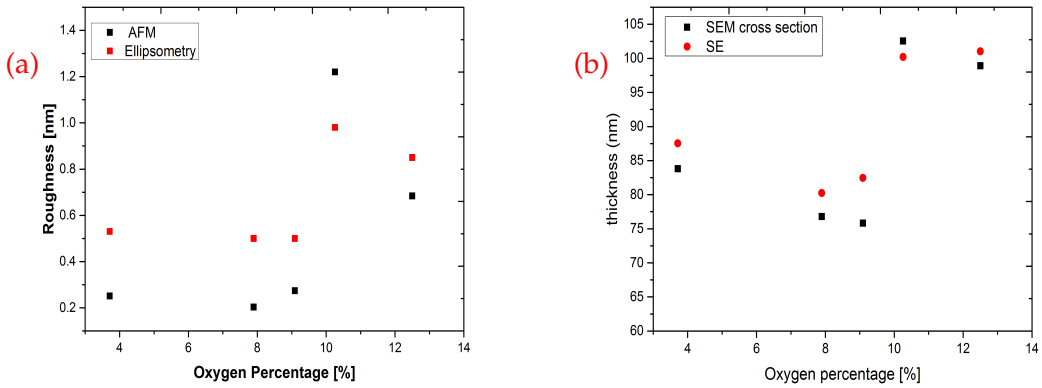

FIGURE 4.16: Modelled and measured a) RMS b) thickness as a function of the oxygen percentage for pulsed DC deposited films

material, hence they can be used to evaluate the change of the optical response with respect to the film growth parameters.

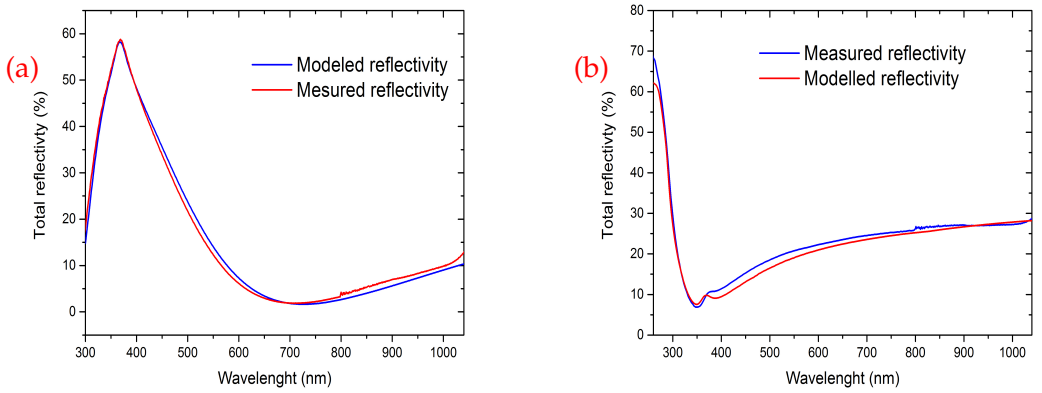

FIGURE 4.17: Modelled and measured reflectivity of ZrO_2 deposited on Si(100) substrate using a) pulsed DC b) RF reactive magnetron sputtering.

The evolution of the refractive index with respect to the oxygen percentage in the chamber is represented in figure 4.18. The increase of the oxygen percentage has the consequence of reducing the refractive index (n). However, the value of n tends to saturate as the oxygen percentage increases. This behaviours is related to the increase of the band gap energy, since the refractive index is related to the probability of the interband transition by :

$$n = \left[1 + 8\pi N(\epsilon)e^2 \quad \sum_{j=1}^{\infty} \frac{|< \phi_j|H|\phi_0 >|^2}{E_j - E_0}\right]^{1/2} \tag{4.2}$$

where N(ϵ) is the electron density of state, e is the charge of an electron ϕ_j and ϕ_0 are the wave function of the excited and the ground states respectively, $E_j - E_0 = E_g$ is

the band gap energy. From equation 4.2 if one assume that the electron density is constant, the refractive index is decreased only with the increase of $E_j - E_0$ quantity. The band gap itself depends on several factors such as (temperature , crystalline structure , crystalline orientation etc...).

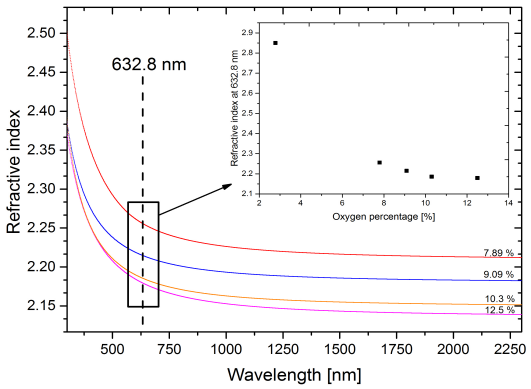

FIGURE 4.18: Variation of the refractive index with respect to the wavelength. The insert shows the variation of the refractive index at 632.8 nm as a function of oxygen percentage

To determine the optical band gap equation 3.13 was used assuming a direct transition. Figure 4.19 shows a plot of $(\alpha h\nu)^{1/2}$ vs photon energy. The intersection of the interpolated linear part of the curve and the photon energy axis gives the value of the optical gap. The obtained values are reported in the insert plot of figure 4.19. An increase of the optical gap with increased oxygen percentage is observed and a maximum value of 4.86 eV is obtained. This value is within the range of the reported value in the literature [45, 67, 52].

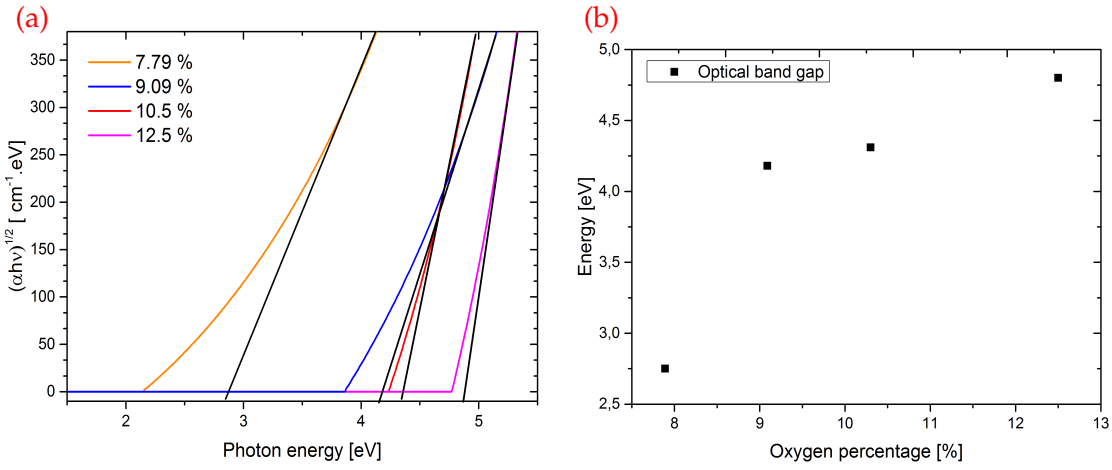

FIGURE 4.19: a) $(\alpha h\nu)^{1/2}$ vs photon energy for pulsed DC deposited ZrO_2 films. The intersection indicate the band gap value and b) the variation of the optical gap with respect to the oxygen percentage in the chamber.

For the RF deposited films the same procedure of fitting experimental and modelled ellipsometry data was followed. The obtained roughness and thickness from SE are in

very good agreement with the measured roughness from AFM and the thickness determination from the SEM cross section. The measured and the modelled reflectivities for one of the deposited films at 9% oxygen in the chamber is shown in figure 4.17, which shows again that the build Tauc-Lorentz function can be trusted to describe with accuracy the properties of the film. The obtained refractive index at 632.8 nm are lower then the ones obtained for pulsed DC deposited films. The variation of the refractive index with respect to the wavelength and oxygen percentage are presented in figure 4.20a. The behaviour of the refractive index with the oxygen percentage shows a decrease of n as the oxygen percentage increases.

A minimum n value of 1.88 was obtained for the film deposited at 11 % of oxygen in the chamber. The low refractive index obtained using RF is lower than the DC deposited film and this difference was attributed to the change of the packing density of the film [2]. However, from the obtained SEM cross section (see figure 4.12) the density of the both films prepared by the two techniques looks similar. This difference can also be attributed to the different crystalline phase that was observed for pulsed DC deposited film.

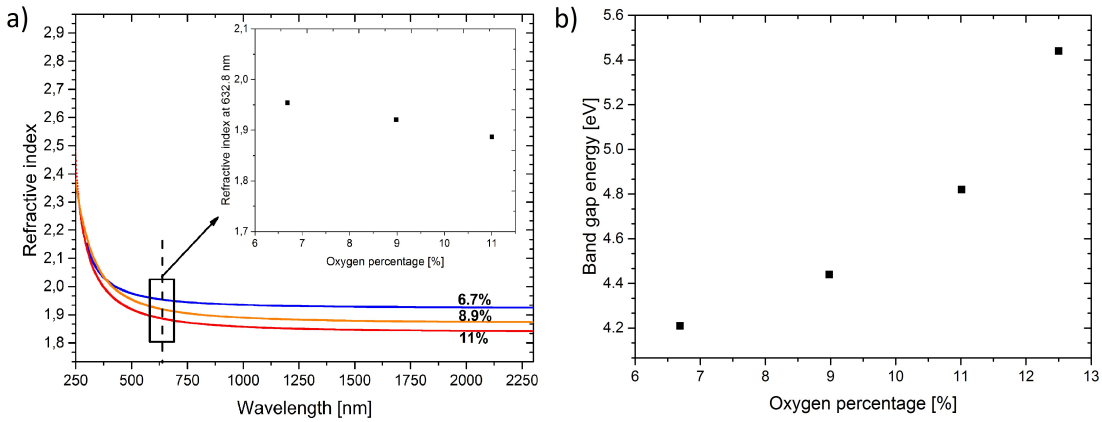

FIGURE 4.20: a) Variation of the refractive index with respect to the wavelength. The insert shows the variation of the refractive index at 632.8 nm as a function of the oxygen percentage b) Variation of the optical gap with increasing oxygen percentage

To conclude the study of the optical properties of the RF deposited film, figure 4.20 shows the variation of the optical gap energy with respect to the oxygen percentage. The band gap energy tend to increase with increasing oxygen percentage. The trend of this later can not be explain by the change in the crystalline structure because it was found to be similar for all films. However, we expect that the increase of the crystalline size might affect the band gap energy. Furthermore, a high optical band gap of a value of 5.44 eV was obtained. This value are extremely similar to the gap value determined from valence band measurement using XPS but also the reported by [24]. This will discussed in more detail in section 4.1.5.

Summary

Several metallic materials has been deposited and characterized to fit the purpose of there application for ITER. The deposition of Rh using RF magnetron sputtering seems to give a better defined structure then the one reported using pulsed DC. The Aluminium deposited films have shown to be oxygen free which is very necessary for

high reflectivity. Different classes of ZrO_2 thin film using both pulsed DC and RF reactive magnetron sputtering were deposited . The influence of the oxygen percentage defined as $O_2\% = \frac{P_{O2}}{P_{TOT}}$ on the structural, optical and morphology of the deposited films was carried out by using XRD,SEM,AFM and ellipsometry. We showed that the crystalline structure changes for the pulsed DC deposited films if increasing the oxygen percentage in the chamber, while the roughness stays relatively low. we reported a maximum value of RMS value of 1.25 nm. For the RF deposited films the crystalline structure does not change with increasing the oxygen percentage and this is attributed to the low deposition rate which gives enough time for the adatom to find an equilibrium position. A maximum RMS value of 2.5 nm is recorded for RF deposited films. For ITER application a high total reflectivity and low diffuse reflectivity of the mirror is one of the requirement. The optical studies showed that the RF deposited film have a low refractive index. This films when is deposited on Al substrate will act as a transparent coating. Due to the high reflectivity of the Al the mirror will have a required optical properties to fill up the criteria of ITER conditions. The difference of RMS for both deposited films using both techniques does not increase dramatically the diffuse reflectivity as we will see later on. Further more to validate weather pulsed DC or RF deposition technique will be used to coat FM's one should experimentally evaluate the effect of ion bombardment on ZrO_2 this will be also described at the end of this report.

4.1.5 Tailoring electronic properties of ZrO2 and charge correction of XPS spectra

Zirconium dioxide thin films were analysed using XPS technique. The obtained spectra of O1s and Zr3d together with the Auger lines emission and the valence band were recorded for each film. Before giving the measured binding energy and valence band position we would like to remind that because of the insulator nature of the deposited films a build up of a static charge at the surface causes the shift of the measured spectra. The most common way to correct the shift in the binding energy is either by calculating the auger parameter defined in equation 4.3 [39] or by taking C1s peak as a reference.

$$\alpha' = BE(Zr3d_{3/2}) + KE(ZrM_{45}N_1N_{23}) \tag{4.3}$$

where α' is the auger parameter, $BE(Zr3d_{5/2})$ is the binding energy of Zr3d$_{3/2}$ and $KE(ZrM_{25}N_1N_{23})$ is the kinetic energy of MNN ejected Auger electron. The problem of the auger parameter is the need of a reference sample. Furthermore, it should be reminded that the auger parameter can only be trustful in the case where the relaxation shift is poor. one should keep in mind that the binding energy of an element depend on potential of the environment that it experience (the crystalline structure and crystalline orientation etc..). In this section we intend to demonstrate the ability of charge correction based on the auger transitions that involve the valence band such as $ZrM_{45}N_1V$ auger transitions for a metallic film partially oxide and a fully oxide films and link the corrected BE to the structure of the film.

Let us first examine the valence band, Auger lines, and BE of the elements for a partially oxidized film. For this type of film due to its conducting properties, the sample does not experience any static charges. In figure 4.21c the BE of core level $Zr3d_{5/2}$, $Zr3d_{3/2}$ is presented. The peak of $Zr3d$ was de-convoluted to three sub-peaks which correspond to metallic and sub-oxides located at 178.64 eV ,179.54 eV and 180.44 eV. The spin-orbit splitting is 2.4 eV and the intensity ratio of $Zr3d_{5/2}$ and $Zr3d_{3/2}$ is 0.66.

The obtained values of BE show that the film is mainly metallic and the shift of about 0.9 eV per metal-suboxide are observed and they are in agreement with the values found in the literature [35]. For the recorded peak of O1s figure (4.21d) an existence of two peaks were detected. The main peak centred at 531.01 eV is attributed to the chemically adsorbed oxygen [57] and the broad peak at higher BE is attributed to hydroxyl species (OH^-). The auger transitions for metallic zirconium are shown in figure 4.21.a $M_{45}(M)N_1(M)N_{23}(M)$,$M_{45}(M)N_{23}(M)N_{23}(M)$, $M_{45}(M)N_1(M)V(M)$ and $M_{45}(M)N_{23}(M)V(M)$ (where M stand up for metallic) was measured and found to be located at 91.6 eV ,114.6 eV, 127.7 eV and 149.6 eV respectively. The obtained values are found to be in good agreement with [61] , a slight difference is attributed to low oxidation state found by fitting XPS data. From fig 4.21.b the measured valence band shows the existence of Zr 4d aligned at the Fermi level and a low intensity peak attributed to O 2p band. Since the shape of valence spectra is proportional to the density of state and because the intensity of the auger line MNV is by itself proportional to the transition probability which involve the valence density of state. The lower O 2p intensity is direct consequence of the low intensity peak of auger line existence at 143.4 eV.

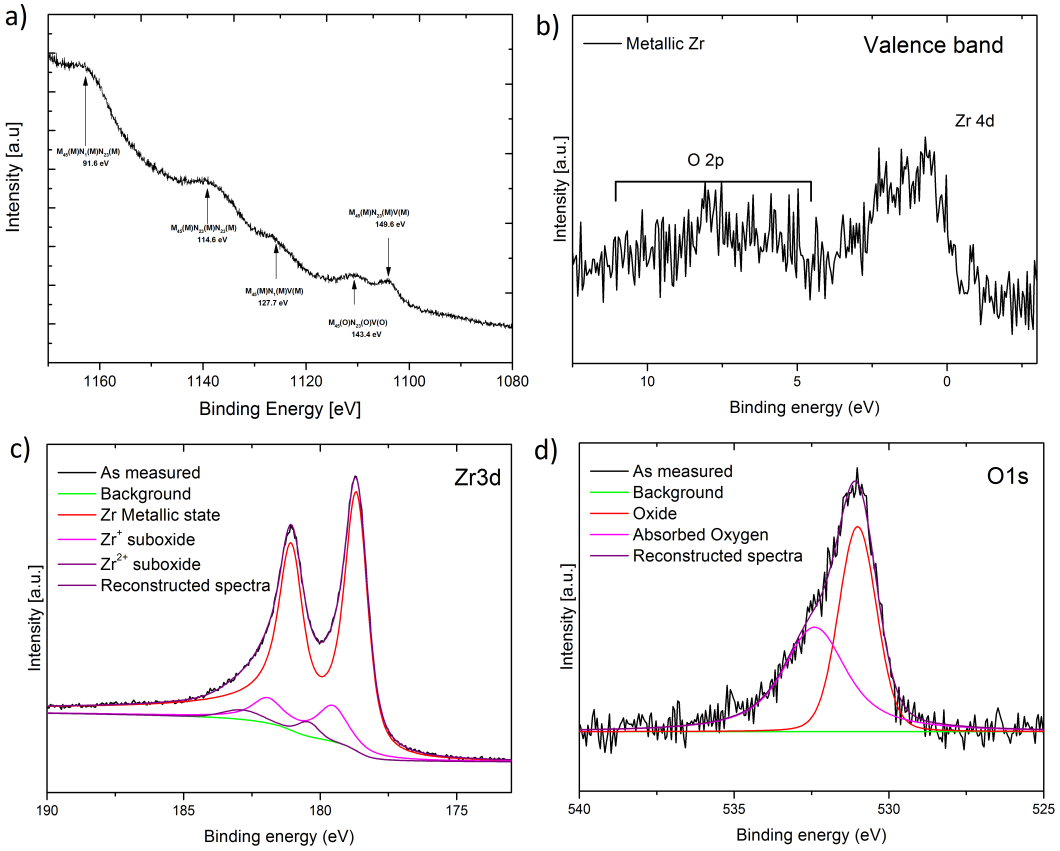

FIGURE 4.21: a)Auger lines. b) Valence band c) core level $Zr3d$ and c) core level $O1s$ measured using XPS of a metallic film

The question that we want to answer is whether the effect of the sample charging can be corrected simply using the auger lines which involve the valence transitions and where the conduction band is located after the formation of ZrO_2. Several authors assume that the bottom of the conduction band is located at 0 eV and that the band gap will be only the difference $0 - E_{UVB}$ where E_{UVB} is the energy of the upper valence

band. To answer these questions, we first need to know what are the properties and the mechanism that involves each region of the XPS spectra.

The Zr MNN auger peak exhibit very attractive properties because they involve valence bands which are very sensitive to bonding configuration and hence display a shift with changing environment. However, the MNV peaks are affected by the change of the Zr4d density of state while the core levels are hardly affected [29]. For lower oxidation states in a metallic matrix , the density of state of O2p and Zr4d gives rise to two auger transition $M_{45}(M)N_{23}(M)V(M)$ and $M_{45}(O)N_{23}(M)V(O)$ (the letter O stand for oxide) at 143.4 eV and 149.6 eV respectively. The increase of the oxygen percentage in the film has as an effect the increase of the O2p density of state which explain the increase of the intensity of the auger lines. The split of the auger peaks of $M_{45}(M)N_{23}(M)V(M)$ and $M_{45}(O)N_{23}(M)V(O)$ is found to be 5.8 eV. This value of the split of the auger lines is surprisingly similar (5.7 eV) for the shift of kinetic energy from the metallic ZrMNV to ZrO2 MNV reported by [29]. In the same time the transition from a metallic like film to an oxide film causes the disappearance of $M_{45}(M)N_{23}(M)V(M)$ in favour of $M_{45}(O)N_{23}(M)V(O)$ (see figure 4.22.a).

We could take the $M_{45}(O)N_{23}(M)V(O)$ peak position of the metallic film with low concentration of oxygen as reference peak for the shift correction. This procedure has been developed assuming that once the O2p band is constructed the auger transition involving valence band does not shift from sub-oxide to an oxide. This assumption is very strong, but as we will show in section 4.1.6 the depletion of an oxide film from oxygen does not shift the O 2p band to higher value. Based on this results the spectra of oxide films was shifted with respect to partially oxidized film. The binding energy of $Zr3d_{5/2}$ and $Zr3d_{3/2}$ of the deposited ZrO_2 films using RF are found to be located at 181.8 eV and 184.2 eV respectively, in perfect agreement with [34]. From figure 4.22c we noticed that the introduction of a low percentage of oxygen leads to the full oxidation of the film. This can be explained by the low deposition rate (0.8 Å/s) which gives enough time for the oxidation to take place and as shown before the crystalline structure stays the same. Moreover from figure 4.22d the oxygen peak at 531 eV is attributed to the chemisorbed oxygen, the increase of the oxygen percentage in the chamber causes a shift of the O1s peak to 529.7 eV which originated from stoichiometric ZrO_2. Third oxygen peak is observed at higher energy 532.4 eV is assigned to the absorbed oxygen on the surface.

From the measured auger peaks and valence spectra we noticed a shift in the kinetic energy and binding energy between the metallic and oxide films. The origin of the shift in both auger peaks and valence bands is different . As explained before in auger peaks the shift of the core levels is due to the chemical shift caused by a change in the electron configuration surrounding the zirconium atom in the oxide and the relaxation of the core holes in the final state, while the energy shift of the valence band is due to the formation of the oxygen 2p band below the Fermi level by oxide formation. This is shown in 4.22 where for a metallic film the Fermi level is located at 0 eV and the addition of oxygen allows the formation of O 2p band that contain the O2p non-bounding and O-cation hybridized bonding orbitals that extended from 2.5 to 8.5 eV binding energy as the linear-combination-of-atomic-orbitals (OLCAO) predict [15]. The broadening of this region is due to the different inter-band transitions between the O2p states and Zr4d states. The band located at 21.98 eV is attributed to the transition $O2s(VB) \rightarrow Zr4d(CB)$ and this value is in good agreement with the experimental value obtained by [46, 15] for ZrO_2 in monoclinic phase. We observed the rise of Zr^{+2} from the occupied Zr4d located at 16.5 eV. From the metallic to oxide films,a shift of 3 eV of the Zr 4p band is observed. The $Zr4p$ band for the oxide can be seen as a doublet

centred at 30.27 eV and 31.6 eV.

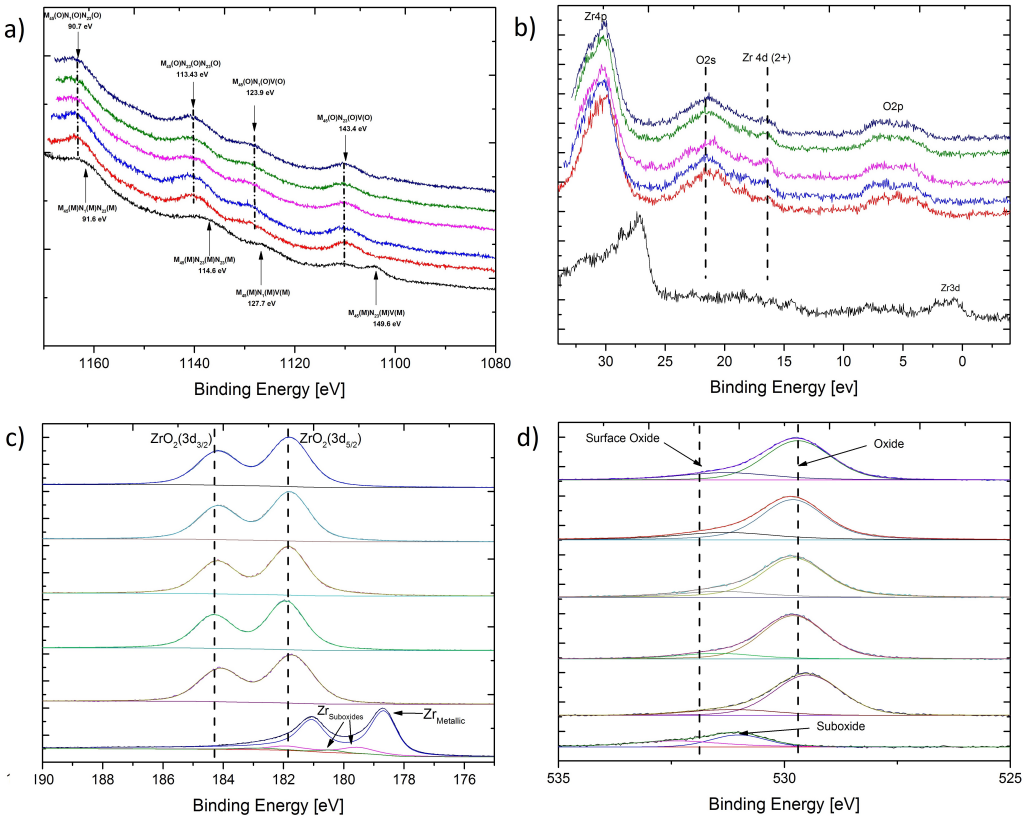

FIGURE 4.22: stacked XPS spectra of a) Auger electrons b) Valence band c) $Zr3d_{5/2}$ and $Zr3d_{3/2}$ d) O1s of metallic and stoichiometric ZrO_2

To further check how good is the approach of taking the auger transition $M_{45}(O)N_{23}(M)V(O)$ in a sub-oxide as a reference value to correct the shift of the spectra due to the charging effect. we exposed one of the oxide sample deposited using RF at 11% oxygen to air to obtain some carbon contamination and we corrected the positions of the peaks using C1s at 284.6 eV as a reference. We used for this experiment a AlK_α x-ray radiation. The results are presented in figure 4.23. After having corrected the shift in BE using both method the BE are similar to the one reported by [21] where the shift in BE was corrected based on the α auger parameter and ZrLMM auger line.

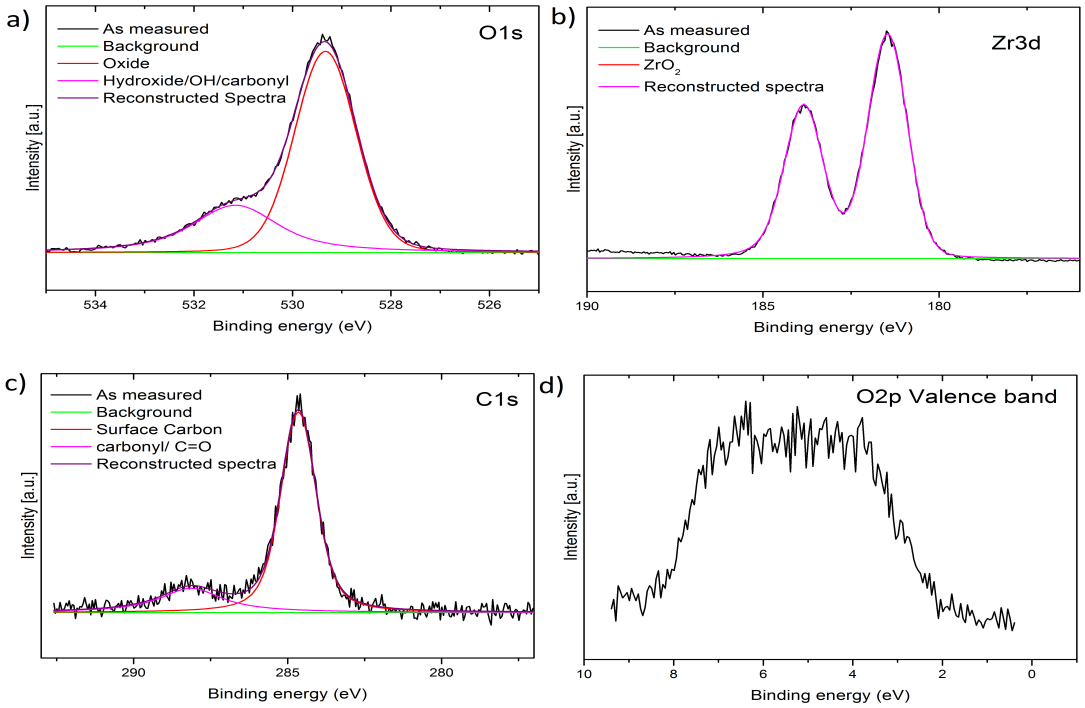

FIGURE 4.23: XPS spectra of a) O1s b) $Zr3d$ c) C1s d) Valence band Oxide film exposed to air

Table 4 gives a summary of the different binding energies using C1s and $M_{45}(O)N_{23}(M)V(O)$ as a reference to shift the spectra. We can clearly see that two approaches gives the same results.

Table 4: comparaison between corection shift using C1s and $M_{45}(O)N_{23}(M)V(O)$ auger line

Peaks	Atomic Concentrations of elements	Using C1s reference [eV] ($\pm 0.2eV$)	Using Zr MNV[a] reference [eV]($\pm 0.2eV$)
$Zr3d_{5/2}$	26.12%	181.4	181.8
$Zr3d_{3/2}$		183.86	184.2
O1s	36.19 %	529.3	529.7
O_1 [b]	14.45%	531.1	531
C1s	18.67 %	284.6	N.A
C_1 [c]	4.56%	288.1	N.A
$E_v - E_f$	–	2.5	2.7

[a] $M_{45}(O)N_{23}(M)V(O)$ [b] Hydroxide/OH/carbonyl [c] carbonyl/ C=O

At the end the UVB (Upper Valence Band) was determined by Unifit software package by fitting the valence band edge. The obtained values with increasing oxygen percentage in the chamber are found to be 2.7 $\pm$ 0.1 eV for all films. Several authors [47, 20] attribute the difference in energy between the first occupied state and the Fermi level supposed to be at 0 eV to the energy gap supposing that the Zr 4d conduction band is located at 0 eV . However it has been shown that the conduction band in polycrystalline zirconium dioxide is located at 2.2 eV below the fermi level measured by Inverse Electron Spectroscopy [6]. While for amorphous ZrO_2 the conduction tail can extend to 1.63 eV as it was calculated and measured in [47]. The energy gap of the deposited film in our case is then determined to be 5 $\pm$ 0.2 eV . This value is found

to be close to the one determined by ellipsometry spectroscopy (5.44 eV) for the film deposited at high oxygen percentage (see section 4.1.4). We have also determined from ellipsometry measurement that there is a variation of the band gap energy with increasing oxygen percentage, which is not seen with XPS analysis. This difference is attributed to the difference in the techniques itself. The XPS is a surface characterization technique and it is scan only a depth of at maximum 5 nm , while ellipsometry is a bulk characterization technique. Since the surface experienced different potential (bulk potential , vacancies and defects) and that under the deposition condition the introduction of the oxygen can lead to formation of a more oxidized film at the surface than at the bulk, this effects can lead to the mismatch of the band gap obtained from ellipsometry and XPS. It is to be noticed that for high oxygen percentage the values are very close, which can be explained by the fact that the existence of enough oxygen in the medium (vacuum chamber) the film is fully oxidized over the hole range of thickness. Similar studies of band gap determination of TiO_2 has shown that the surface can be affected by the reaction with oxygen that leads to a change in the band gap value [11].

Charge correction

After having demonstrated the ability of charge correction using $M_{45}(O)N_{23}(M)V(O)$ auger lines. We corrected the shift of the films deposited using DC pulsed excitation following the same ideas described in the previous section. The films deposited using pulsed DC shows a change in the crystalline orientation and phase with increasing the oxygen percentage in the chamber (see 4.9a). Because the binding energy depend on the crystalline form of the film and surface energy, we attend to show that even with the change in the crystalline structure the $ZrM_{45}(O)N_{23}(M)V(O)$ auger line stay unchanged for a monoclinic and tetragonal phase mixture this argument is supported by the fact that the monoclinic structure has in fact a partly octahedral and partly tetrahedral crystal field and that close to the valence band edges the density of states for all ZrO_2 are similar [42]. Figure 4.25 shows the shift corrected spectra for valence band, Auger lines, $Zr3d$ and O1s regions for different oxygen concentration in the chamber. Contrary to the RF deposited film, the addition of oxygen shows a formation of partially oxide configuration. The $Zr3d$ spectra for a mixture of metallic and oxide states were performed following [37] and an example of the fitted spectra is giving in figure 4.24a , both binding energy of metallic and stoichiometric oxide $Zr3d_{5/3}$ are located at 178.62 eV and 182.48 eV are in perfect agreement with [37].

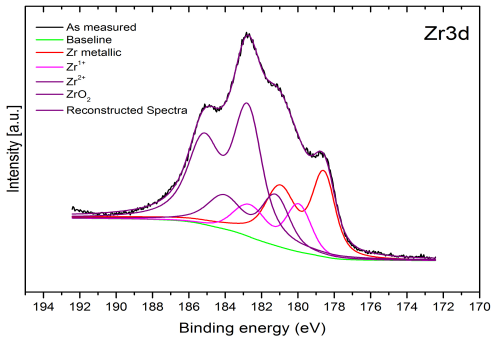

FIGURE 4.24: fitted XPS spectra for partial oxide ZrO_x film

The binding energy of the films having a phase mixture with a tetragonal dominated phase and those with monoclinic phase oriented along (200) are found to be centered at 182.5 eV. This value is higher than the one obtained for RF deposited film. This difference can be explained by the difference in the surface energy along different orientation and phase. Following [46] the surface energy of different phases and orientation of $ZrO2$ was calculated using DFT. It has been shown that for tetragonal phase (101) and monoclinic (100) the surface energies are very closed (2322 and 2283 mJ$/m^2$ respectively) and they are much higher than the monoclinic phase (-111) which was calculated to be 1862 mJ$/m^2$. For the films that show a monoclinic phase (-111) the binding energy is found to be located at 182.25 eV, slightly higher then the films deposited by RF that shows the same phase. This difference can be attributed to the difference of the crystallite size (see figure 4.10) the same effect being shown in [56].

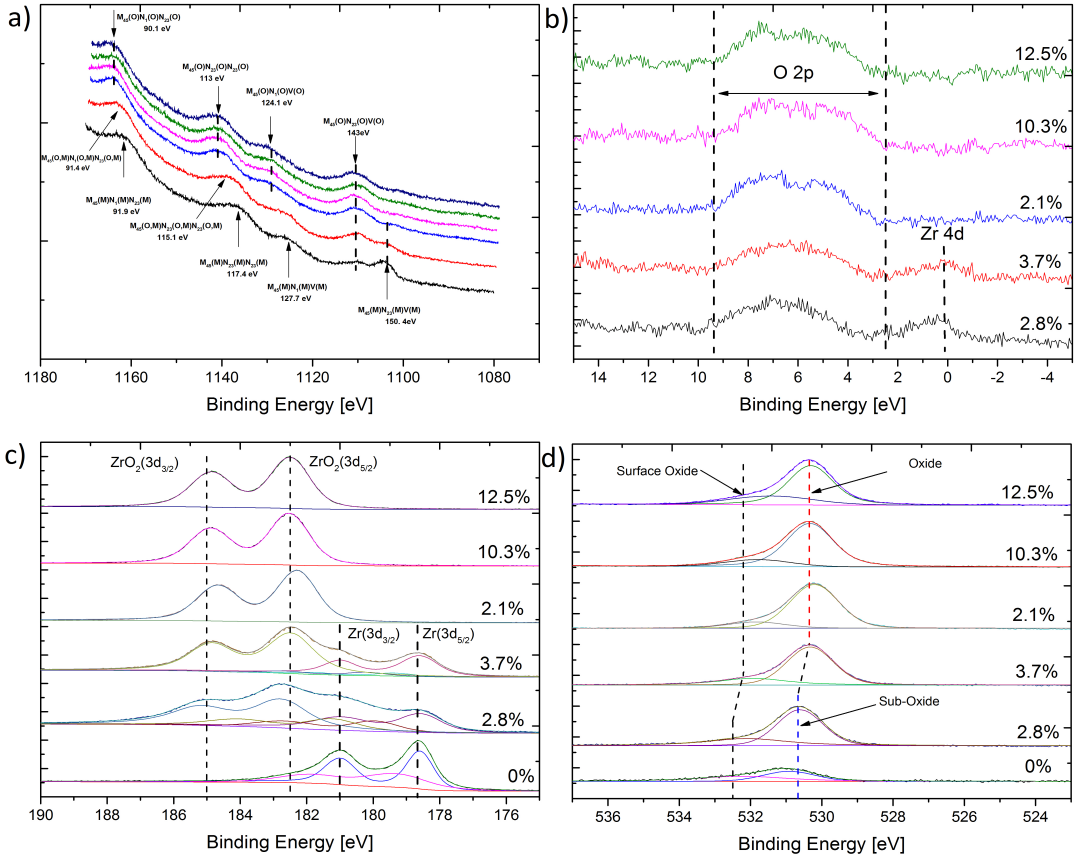

FIGURE 4.25: stacked XPS spectra of a) Auger electrons b) valence band c) $Zr3d_{5/2}$) and $Zr3d_{3/2}$) d) O1s of metallic and Oxide films for different oxygen percentage in the chamber

4.1.6 Effect of Ar+ bombardment on the electronic properties of ZrO_2

A stoichiometric ZrO_2 film was deposited using pulsed DC reactive magnetron sputtering. The change in the electronic properties and composition of ZrO_2 caused by 3 keV Ar^+ bombardment is presented here using core-level spectra measured by XPS and valence band measured by UPS. The results as it will be shown are complementary to [38], where it has been suggested that the O 2p valence band region is fairly sensitive to

Ar^+ sputtering. However no definitive conclusion has been drown , since the authors suggested that due to the low photo-emission cross section of the VB their detection revealed to be difficult. The use of UPS allows to probe at most 1 nm depth. Because the surface will be subject to ion bombardment , any defect in the surface inducing electronic defects will be detected.

Figure 4.26 shows the UPS spectra after each cycle of Ar^+. For the freshly deposited ZrO_2 film the valence band shows a peak located at 5.34 eV and a shoulder located at 9.14 eV. They are assigned to the oxygen bonding and non-bounding orbitals. The broaded peak centred at 14.5 eV is attributed to $Zr4d(2^+)$ that arises for Zr 4d occupied states. A low intensity peak is observed at 3.12 ev and is attributed to defect states in the band gap. The valence band maximum is located at $\sim$ 4.1 eV below the Fermi level and was determined by the least square fit method. The peak located at 3.35 eV is attributed to the positively charge defect in the band gap and it is in perfect agreement with the value calculated using density functional theory in monoclinic zirconia [14].

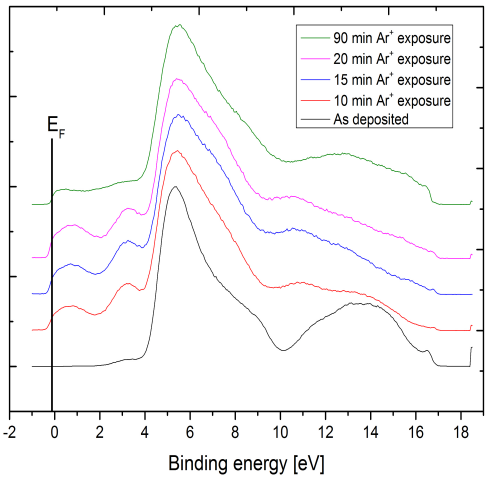

FIGURE 4.26: fitted XPS spectra for partial oxide ZrO_x film

The exposure of the ZrO_2 film to 3 keV Ar^+ for different time shows the appearance of new features. The increase of the intensity of the peak attributed to positively charge defect shows that the sputtering process increase the density of the defect states due to the preferential sputtering of oxygen atoms. Furthermore, a new peak appears at 0 eV which might be attributed to Zr4d conduction band. The origin of the disappearance of the peak located at 14.5 eV with sputtering is not clear. A shift of the shoulder located at $\sim$ 9.14 ev to $\sim$ 7.4 eV with an increase of the intensity is observed, this can be interpreted as an increase of the O 2p non-bounding type orbitals which causes the appearance of lower oxidation states in XPS spectra (see figure 4.27). A more important effect it that the O 2p shows no changing in the position confirming that they are not sensitive to the Ar bombardment nor to oxidation of the film. After 90 min sputtering we detected the Si2p coming from the substrate. From UPS spectra at 90 min we observed a broadening of a low intensity peak from 0 eV to $\sim$ 4 eV. This might be due Si-ZrO_x interface defect . A reappearance of a broaded peak around $\sim$ 12 eV is attributed to Si $3d3sO2p$ hybridised states [65].

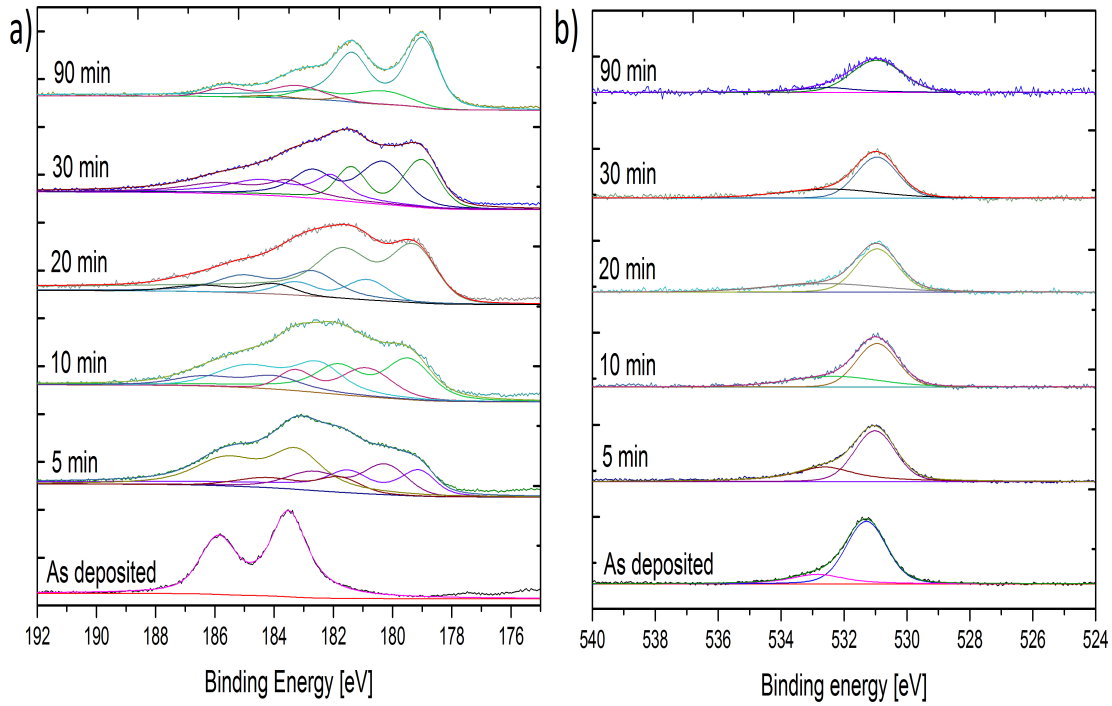

FIGURE 4.27: Variation of the cor-level spectra as a function of the sputtering time at 3 keV

Chapter 5

General conclusion

In this present work, we have demonstrated that the use of auger lines which involves valence band transition in a low oxide film, can be taken as a reference value to correct the shift of BE due to the charging of the sample. This method seems to be in very good agreement with the often used method namely the defined auger parameter and carbon C1s peak. Based on the obtained results for valence band, the band gap was determined and correlated to the optical band gap. Similar value was obtained for films deposited at high oxygen percentage in the chamber. The mismatch of band gap for films obtained from ellipsometry and XPS for lower oxygen percentage has been attributed to higher oxidation of the surface with respect to the bulk. The correlation between the BE and crystalline structure has also been investigated. We showed that due to the similar surface energies of the monoclinic and tetragonal phase the BE do not change. However, the change in the crystalline size was demonstrated to affect the binding energies.

The deposited films were tuned to fits the optical , electrical and morphology properties for ITER. The selected coating conditions was picked up to coat SS-Al system. The effect of Ar^+ bombardment on the electronic structure , optical properties on the film was studied. We showed that the Ar bombardment increase the density of the defect states which might cause a absorption at the photon energy of 3.33 eV that could be a disadvantage in plasma cleaning technology for ITER. However, the relatively low oxygen pressure in ITER might solve this issue. The availability of oxygen in the surrounding media might decrease the defect state due to the reaction of the oxygen with the surface of ZrO_2.

To validate this vision several experiment was conducted using RF plasma cleaning and it show that due to the sputtering of the adsorbed oxygen from the walls of the deposition chamber, the film has conserved it stoichiometry. The result of this studies are not shown in this present report and will be a subject of further studies.

Bibliography

[1] Venkataraj et al. "Structural and optical properties of thin zirconium oxide films prepared by reactive direct current magnetron sputtering". In: *Journal of Applied Physics* 92.7 (2002).

[2] S Ben Amor et al. "Characterization of zirconia films deposited by rf magnetron sputtering". In: *Materials Science and Engineering: B* 57.1 (1998), pp. 28–39.

[3] S. Berg, E. SÃd'rhammar, and T. Nyberg. "Upgrading the âĂIJBerg-modelâĂİ for reactive sputtering processes". In: *Thin Solid Films* 565 (2014), pp. 186 –192. ISSN: 0040-6090. DOI: http://dx.doi.org/10.1016/j.tsf.2014.02.063. URL: http://www.sciencedirect.com/science/article/pii/S0040609014001989.

[4] S Berg et al. "Modeling of reactive sputtering of compound materials". In: *Journal of Vacuum Science & Technology A* 5.2 (1987), pp. 202–207.

[5] Sören Berg and Tomas Nyberg. "Fundamental understanding and modeling of reactive sputtering processes". In: *Thin solid films* 476.2 (2005), pp. 215–230.

[6] Eric Bersch et al. "Band offsets of ultrathin high-κ oxide films with Si". In: *Phys. Rev. B* 78 (8 2008), p. 085114. DOI: 10.1103/PhysRevB.78.085114. URL: http://link.aps.org/doi/10.1103/PhysRevB.78.085114.

[7] DC Carter, RL Arent, and DJ Christie. "Sputter process enhancement through pulsed-DC power". In: *PROCEEDINGS OF THE ANNUAL TECHNICAL CONFERENCE-SOCIETY OF VACUUM COATERS*. Vol. 50. 2007, p. 210.

[8] Dipankar Chattarji. *The theory of Auger transitions*. Elsevier, 2012.

[9] J. Danroc, A. Aubert, and R. Gillet. "Reactive magnetron sputtering of TiN: Analysis of the deposition process". In: *Surface and Coatings Technology* 33.0 (1987), pp. 83 –90. ISSN: 0257-8972. DOI: http://dx.doi.org/10.1016/0257-8972(87)90179-4. URL: http://www.sciencedirect.com/science/article/pii/0257897287901794.

[10] Diederik Depla et al. "Hysteresis behavior during reactive magnetron sputtering of Al2O3 using a rotating cylindrical magnetron". In: *Journal of Vacuum Science & Technology A* 24.4 (2006), pp. 934–938.

[11] Christian Dette et al. "TiO2 Anatase with a Bandgap in the Visible Region". In: *Nano Letters* 14.11 (2014). PMID: 25252265, pp. 6533–6538. DOI: 10.1021/nl503131s. eprint: http://dx.doi.org/10.1021/nl503131s. URL: http://dx.doi.org/10.1021/nl503131s.

[12] A.V. Durov, Y.V. Naidich, and B.D. Kostyuk. "Investigation of interaction of metal melts and zirconia". English. In: *Journal of Materials Science* 40.9-10 (2005), pp. 2173–2178. ISSN: 0022-2461. DOI: 10.1007/s10853-005-1928-5. URL: http://dx.doi.org/10.1007/s10853-005-1928-5.

[13] M W Finnis. "The theory of metal - ceramic interfaces". In: *Journal of Physics: Condensed Matter* 8.32 (1996), p. 5811. URL: http://stacks.iop.org/0953-8984/8/i=32/a=003.

[14] AS Foster et al. "Structure and electrical levels of point defects in monoclinic zirconia". In: *Physical Review B* 64.22 (2001), p. 224108.

[15] R. H. French et al. "Experimental and theoretical determination of the electronic structure and optical properties of three phases of ZrO_2". In: *Phys. Rev. B* 49 (8 1994), pp. 5133–5142. DOI: 10.1103/PhysRevB.49.5133. URL: http://link.aps.org/doi/10.1103/PhysRevB.49.5133.

[16] Hiroyuki Fujiwara. *Spectroscopic ellipsometry: principles and applications*. John Wiley & Sons, 2007.

[17] Ricardo García. *Amplitude modulation atomic force microscopy*. John Wiley & Sons, 2011.

[18] C Giacovazzo et al. "Fundamentals of crystallography (IUCr Texts on Crystallography No. 2.)" In: *Acta Cryst* 49 (1993), pp. 373–374.

[19] Tetsuya Goto, Takaaki Matsuoka, and Tadahiro Ohmi. "Rotation magnet sputtering: Damage-free novel magnetron sputtering using rotating helical magnet with very high target utilization". In: *Journal of Vacuum Science & Technology A* 27.4 (2009), pp. 653–659.

[20] Vladimir Gritsenko et al. "Atomic and electronic structures of amorphous ZrO2 and HfO2 films". In: *Microelectronic Engineering* 81.2âĂŞ4 (2005). The Proceedings of the 2nd International Symposium on Nano- and Giga-Challenges in MicroelectronicsThe Proceedings of the 2nd International Symposium on Nano- and Giga-Challenges in Microelectronics, pp. 524 –529. ISSN: 0167-9317. DOI: http://dx.doi.org/10.1016/j.mee.2005.03.056. URL: http://www.sciencedirect.com/science/article/pii/S0167931705001322.

[21] M. J. Guittet, J. P. Crocombette, and M. Gautier-Soyer. "Bonding and XPS chemical shifts in $ZrSiO_4$ versus SiO_2 and ZrO_2 : Charge transfer and electrostatic effects". In: *Phys. Rev. B* 63 (12 2001), p. 125117. DOI: 10.1103/PhysRevB.63.125117. URL: http://link.aps.org/doi/10.1103/PhysRevB.63.125117.

[22] G He et al. "Structural, interfacial and optical characterization of ultrathin zirconia film grown by in situ thermal oxidation of sputtered metallic Zr films". In: *Nanotechnology* 16.9 (2005), p. 1641. URL: http://stacks.iop.org/0957-4484/16/i=9/a=040.

[23] George Hohlneicher, Harald Pulm, and Hans-Joachim Freund. "On the separation of initial and final state effects in photoelectron spectroscopy using an extension of the auger-parameter concept". In: *Journal of electron spectroscopy and related phenomena* 37.2 (1985), pp. 209–224.

[24] M. Houssa et al. "Variation in the fixed charge density of SiOx/ZrO2 gate dielectric stacks during postdeposition oxidation". In: *Applied Physics Letters* 77.12 (2000).

[25] Igor Iatsunskyi et al. "Structural and {XPS} characterization of {ALD} Al2O3 coated porous silicon". In: *Vacuum* 113 (2015), pp. 52 –58. ISSN: 0042-207X. DOI: http://dx.doi.org/10.1016/j.vacuum.2014.12.015. URL: http://www.sciencedirect.com/science/article/pii/S0042207X14004114.

[26] D Ivanova et al. “An overview of the comprehensive First Mirror Test in JET with ITER-like wall”. In: *Physica Scripta* 2014.T159 (2014), p. 014011. URL: http://stacks.iop.org/1402-4896/2014/i=T159/a=014011.

[27] G. E. Jellison and F. A. Modine. “Parameterization of the optical functions of amorphous materials in the interband region”. In: *Applied Physics Letters* 69.3 (1996).

[28] Haikun Jia et al. “ANALYSIS OF STABILITY OF STRAIGHT SIDE BUCKLES ON ELASTIC SUBSTRATES”. In: ().

[29] B. Jungblut, G. Sicking, and T. Papachristos. “The oxidation of zirconium as observed by Auger electron spectroscopy: A comparison of experiment and density of state calculations”. In: *Surface and Interface Analysis* 13.2-3 (1988), pp. 135–141. ISSN: 1096-9918. DOI: 10.1002/sia.740130205. URL: http://dx.doi.org/10.1002/sia.740130205.

[30] P. J. Kelly et al. “Reactive pulsed magnetron sputtering process for alumina films”. In: *Journal of Vacuum Science & Technology A* 18.6 (2000).

[31] Yang Leng. *Materials characterization: introduction to microscopic and spectroscopic methods*. John Wiley & Sons, 2009.

[32] Michael A Lieberman and Allan J Lichtenberg. “Principles of plasma discharges and materials processing”. In: *MRS Bulletin* 30 (1994), pp. 899–901.

[33] LD Lucas. “Techniques de l’Ingénieur”. In: *Paris M67* (1984), p. 1.

[34] Debasis Majumdar and Dilip Chatterjee. “XâĂŘray photoelectron spectroscopic studies on yttria, zirconia, and yttriaâĂŘstabilized zirconia”. In: *Journal of Applied Physics* 70.2 (1991).

[35] L Marot et al. “Characterization of magnetron sputtered rhodium films for reflective coatings”. In: *Surface and Coatings Technology* 202.13 (2008), pp. 2837–2843.

[36] Noriaki Matsunami et al. “Energy dependence of the ion-induced sputtering yields of monatomic solids”. In: *Atomic Data and Nuclear Data Tables* 31.1 (1984), pp. 1 –80. ISSN: 0092-640X. DOI: http://dx.doi.org/10.1016/0092-640X(84)90016-0. URL: http://www.sciencedirect.com/science/article/pii/0092640X84900160.

[37] C. Morant et al. “An {XPS} study of the interaction of oxygen with zirconium”. In: *Surface Science* 218.2âĂŞ3 (1989), pp. 331 –345. ISSN: 0039-6028. DOI: http://dx.doi.org/10.1016/0039-6028(89)90156-8. URL: http://www.sciencedirect.com/science/article/pii/0039602889901568.

[38] C Morant et al. “Electronic structure of stoichiometric and Ar+-bombarded ZrO 2 determined by resonant photoemission”. In: *Physical Review B* 52.16 (1995), p. 11711.

[39] Giuliano Moretti. “Auger parameter and Wagner plot in the characterization of chemical states by X-ray photoelectron spectroscopy: a review”. In: *Journal of Electron Spectroscopy and Related Phenomena* 95.2âĂŞ3 (1998), pp. 95 –144. ISSN: 0368-2048. DOI: http://dx.doi.org/10.1016/S0368-2048(98)00249-7. URL: http://www.sciencedirect.com/science/article/pii/S0368204898002497.

[40] L. Moser et al. “Towards plasma cleaning of ITER first mirrors”. In: *Nuclear Fusion* 55.6 (2015), p. 063020. URL: http://stacks.iop.org/0029-5515/55/i=6/a=063020.

[41] B.A. Movchan and A.V. Demchishin. "STRUCTURE AND PROPERTIES OF THICK CONDENSATES OF NICKEL, TITANIUM, TUNGSTEN, ALUMINUM OXIDES, AND ZIRCONIUM DIOXIDE IN VACUUM." In: *Fiz. Metal. Metalloved. 28: 653-60 (Oct 1969).* (1969).

[42] MC Munoz et al. "Adhesion at metal–ZrO 2 interfaces". In: *Surface Science Reports* 61.7 (2006), pp. 303–344.

[43] Tadayoshi Ono, Takahiro Kenmotsu, and Tetsuya Muramoto. "Simulation of the Sputtering Process". English. In: *Reactive Sputter Deposition*. Ed. by Diederik Depla and Stijn Mahieu. Vol. 109. Springer Series in Materials Science. Springer Berlin Heidelberg, 2008, pp. 1–42. ISBN: 978-3-540-76662-9. DOI: 10.1007/978-3-540-76664-3_1. URL: http://dx.doi.org/10.1007/978-3-540-76664-3_1.

[44] A. L. Patterson. "The Scherrer Formula for X-Ray Particle Size Determination". In: *Phys. Rev.* 56 (10 1939), pp. 978–982. DOI: 10.1103/PhysRev.56.978. URL: http://link.aps.org/doi/10.1103/PhysRev.56.978.

[45] LO Prieto-López et al. "Optical properties of Zr and ZrO 2 films deposited by laser ablation". In: *Microelectronics Journal* 39.11 (2008), pp. 1371–1373.

[46] Ragesh Puthenkovilakam, Emily A. Carter, and Jane P. Chang. "First-principles exploration of alternative gate dielectrics: Electronic structure of ZrO_2/Si and $ZrSiO_4$/Si interfaces". In: *Phys. Rev. B* 69 (15 2004), p. 155329. DOI: 10.1103/PhysRevB.69.155329. URL: http://link.aps.org/doi/10.1103/PhysRevB.69.155329.

[47] J.M. Sam et al. "A resonant photoemission study of the ZrO2 valence band". In: *Surface Science* 307âĂŞ309, Part B (1994). Proceedings of the European Conference on Surface Science, pp. 848 –853. ISSN: 0039-6028. DOI: http://dx.doi.org/10.1016/0039-6028(94)91502-4. URL: http://www.sciencedirect.com/science/article/pii/0039602894915024.

[48] Caroline A Schneider, Wayne S Rasband, and Kevin W Eliceiri. "NIH Image to ImageJ: 25 years of image analysis". In: *Nature methods* 9.7 (2012), pp. 671–675.

[49] T.K. Sham and M.S. Lazarus. "X-ray photoelectron spectroscopy (XPS) studies of clean and hydrated TiO2 (rutile) surfaces". In: *Chemical Physics Letters* 68.2âĂŞ3 (1979), pp. 426 –432. ISSN: 0009-2614. DOI: http://dx.doi.org/10.1016/0009-2614(79)87231-0. URL: http://www.sciencedirect.com/science/article/pii/0009261479872310.

[50] E. Sharhammar et al. "A study of the process pressure influence in reactive sputtering aiming at hysteresis elimination". In: *Surface and Coatings Technology* 232.0 (2013), pp. 357 –361. ISSN: 0257-8972. DOI: http://dx.doi.org/10.1016/j.surfcoat.2013.05.035. URL: http://www.sciencedirect.com/science/article/pii/S0257897213004799.

[51] Jai Singh. *Optical properties of condensed matter and applications*. Vol. 6. John Wiley & Sons, 2006.

[52] Z. Song, B. R. Rogers, and N. D. Theodore. "Spectroscopic ellipsometry characterization of ZrO2 films on Si(100) deposited by high-vacuum-metalorganic chemical vapor deposition". In: *Journal of Vacuum Science & Technology A* 22.3 (2004).

[53] A.G. Spencer, R.P. Howson, and R.W. Lewin. "Pressure stability in reactive magnetron sputtering". In: *Thin Solid Films* 158.1 (1988), pp. 141 –149. ISSN: 0040-6090. DOI: http://dx.doi.org/10.1016/0040-6090(88)90310-0. URL: http://www.sciencedirect.com/science/article/pii/0040609088903100.

[54] John A Thornton. "High rate thick film growth". In: *Annual review of materials science* 7.1 (1977), pp. 239–260.

[55] John A. Thornton and D.W. Hoffman. "Stress-related effects in thin films". In: *Thin Solid Films* 171.1 (1989), pp. 5 –31. ISSN: 0040-6090. DOI: http://dx.doi.org/10.1016/0040-6090(89)90030-8. URL: http://www.sciencedirect.com/science/article/pii/0040609089900308.

[56] S. Tsunekawa et al. "{XPS} study of the phase transition in pure zirconium oxide nanocrystallites". In: *Applied Surface Science* 252.5 (2005), pp. 1651 –1656. ISSN: 0169-4332. DOI: http://dx.doi.org/10.1016/j.apsusc.2005.03.183. URL: http://www.sciencedirect.com/science/article/pii/S0169433205005647.

[57] J. F. van der Veen, F. J. Himpsel, and D. E. Eastman. "Chemisorption-induced $4f$-core-electron binding-energy shifts for surface atoms of W(111), W(100), and Ta(111)". In: *Phys. Rev. B* 25 (12 1982), pp. 7388–7397. DOI: 10.1103/PhysRevB.25.7388. URL: http://link.aps.org/doi/10.1103/PhysRevB.25.7388.

[58] David B Williams and C Barry Carter. "Transmission electron microscopy: a textbook for materials science". In: *Micron* 28.1 (1997), pp. 75–75.

[59] M. Wisse et al. "Laser-assisted cleaning of beryllium-containing mirror samples from {JET} and PISCES-B". In: *Fusion Engineering and Design* 89.2 (2014), pp. 122 –130. ISSN: 0920-3796. DOI: http://dx.doi.org/10.1016/j.fusengdes.2014.01.042. URL: http://www.sciencedirect.com/science/article/pii/S092037961400043X.

[60] HY Wong et al. "Effects of ion beam bombardment on electrochromic tungsten oxide films studied by X-ray photoelectron spectroscopy and Rutherford backscattering". In: *Thin Solid Films* 376.1 (2000), pp. 131–139.

[61] Masahiro Yamamoto et al. "Auger electron, electron energy loss and secondary electron emission spectroscopic studies on the oxidation of zirconium at high temperatures and room temperature". In: *J. Chem. Soc., Faraday Trans.* 87 (10 1991), pp. 1591–1599. DOI: 10.1039/FT9918701591. URL: http://dx.doi.org/10.1039/FT9918701591.

[62] Y. Yamamura, N. Matsunami, and N. Itoh. "Theoretical studies on an empirical formula for sputtering yield at normal incidence". In: *Radiation Effects* 71.1-2 (1983), pp. 65–86. DOI: 10.1080/00337578308218604. eprint: http://dx.doi.org/10.1080/00337578308218604. URL: http://dx.doi.org/10.1080/00337578308218604.

[63] YASUNORI YAMAMURA and HIRO TAWARA. "{ENERGY} {DEPENDENCE} {OF} ION-INDUCED {SPUTTERING} {YIELDS} {FROM} {MONATOMIC} {SOLIDS} {AT} {NORMAL} {INCIDENCE}". In: *Atomic Data and Nuclear Data Tables* 62.2 (1996), pp. 149 –253. ISSN: 0092-640X. DOI: http://dx.doi.org/10.1006/adnd.1996.0005. URL: http://www.sciencedirect.com/science/article/pii/S0092640X96900054.

[64] F. Yubero et al. “Size and shape of supported zirconia nanoparticles determined by x-ray photoelectron spectroscopy”. In: *Journal of Applied Physics* 101.12, 124910 (2007), pp. –. DOI: http://dx.doi.org/10.1063/1.2749482. URL: http://scitation.aip.org/content/aip/journal/jap/101/12/10.1063/1.2749482.

[65] D. A. Zatsepin et al. “XPS analysis and valence band structure of a low-dimensional SiO2/Si system after Si+ ion implantation”. In: *physica status solidi (a)* 208.7 (2011), pp. 1658–1661. ISSN: 1862-6319. DOI: 10.1002/pssa.201026713. URL: http://dx.doi.org/10.1002/pssa.201026713.

[66] Sha Zhao et al. “Thickness-dependent structural and optical properties of sputter deposited ZrO 2 films”. In: *Optical materials* 30.6 (2008), pp. 910–915.

[67] LQ Zhu et al. “Spectroscopic ellipsometry characterization of ZrO 2 thin films by nitrogen-assisted reactive magnetron sputtering”. In: *Materials science in semiconductor processing* 9.6 (2006), pp. 1025–1030.